SLAC-223

SLAC-223

DECAYS OF THE $\psi'(3684)$ TO OTHER CHARMONIUM STATES

Thomas Michael Himel

SLAC-Report No. 223

October 1979

Under Contract with the

Department of Energy

Contract DE-AC03-76SF00515

DECAYS OF THE $\psi'(3684)$ TO OTHER CHARMONIUM STATES

A DISSERTATION

SUBMITTED TO THE DEPARTMENT OF PHYSICS

AND THE COMMITTEE ON GRADUATE STUDIES

OF STANFORD UNIVERSITY

IN PARTIAL FULFILLMENT OF THE

REQUIREMENTS FOR THE DEGREE OF

DOCTOR OF PHILOSOPHY

By

Thomas Michael Himel

December 1979

SLAC-223
UC-34d
(T/E/I)

DECAYS OF THE $\psi'(3684)$ TO OTHER CHARMONIUM STATES*

Thomas Michael Himel

Stanford Linear Accelerator Center

Stanford University, Stanford, California 94305

October 1979

Prepared for the Department of Energy

under Contract Number DE-AC03-76SF00515.

Printed in the United States of America. Available from National Technical Information Service, U.S. Department of Commerce, 5285 Port Royal Road, Springfield, Virginia 22161. Price: Printed copy $6.50; Microfiche $3.00.

---

* Ph.D. dissertation.

DECAYS OF THE $\psi'(3684)$ TO OTHER CHARMONIUM STATES

We report on an experimental study of the decays of the $\psi'(3684)$ to other charmonium states. The decays of 10^6 $\psi'(3684)$'s were observed with the SLAC-LBL Mark II detector at the e^+e^- storage ring SPEAR. Branching ratios have been measured for $\psi'(3684)$ decays to $\gamma\chi$ where the χ decays to $\gamma\psi(3095)$ or to hadrons. An upper limit of 0.13% is set on the branching ratio for $\psi'\to\gamma\chi(3455)\to\gamma\gamma\psi(3095)$; this is a factor of 6 less than the branching ratio measured by a previous less sensitive experiment. We investigate the decay $\psi'\to\gamma\eta_c$, $\eta_c\to$hadrons. The decay $\psi'\to\pi^0\psi$, which violates isospin conservation, is observed with a branching ratio of $(0.15\pm0.06)\%$.

ACKNOWLEDGEMENTS

The success of a big experiment like the Mark II depends on many people contributing to a team effort. I am pleased to acknowledge the members of the SLAC-LBL collaboration for their contributions to the experiment and for the many useful discussions I have had with them. Special thanks go to Marty Breidenbach who taught me much of what I know about hardware, and to Roy Schwitters for his valuable advice. George Trilling has been especially helpful with his advice on methods of analysis, while Fred Gilman and Dave Miller gave valuable theoretical guidance. Finally, I'd like to thank everyone in the group for making my stay at SLAC a pleasant one.

TABLE OF CONTENTS

LIST OF TABLES

LIST OF FIGURES

Chapter I

INTRODUCTION

Since the discovery of the ψ particle in 1974[1] several other related particles have been found. These particles are called charmonium states since the most successful theory explaining them is the charmonium model. This paper gives new experimental results on the existence and properties of these states. First we'll give a brief review of the charmonium system (theory and experiment) as it stood prior to this experiment.

The charmonium model was formed in analogy to the positronium system. A charmed quark and a charmed anti-quark are bound in a potential well. In contrast to the u, d, and s quarks, the charmed quark is so massive that nonrelativistic approximations can be successfully used. Figure 1 shows the states predicted by this model. The masses of the states are determined by the form used for the potential. The form of this potential as r→0 and as r→infinity is inspired by Quantum Chromodynamics, but the potential in the intermediate region is adjusted to give the masses measured by experiments. Each state in the diagram has 3 labels. The atomic physics label is in the form $N^{2S+1}L_J$; where s is the sum of the quark spins (0 or 1); L (S,P,D,F→0,1,2,3) gives the relative orbital

---

[1]J. E. Augustin et al., Phys. Rev. Lett. 33, 1453 (1974); J. J. Aubert et al., Phys. Rev. Lett. 33, 1404 (1974).

angular momentum of the two quarks; J is the sum of $\vec{L}$ and $\vec{S}$, the total spin; and N gives the radial excitation of system. The second label, J^{PC}, gives the total spin, parity, and charge conjugation of the state. The third label gives the experimental mass and name of the particle associated with the level. There are several excellent review papers which give details on the form of the potential and which summarize the predictions of masses and branching ratios.[2]

The experimental status of the charmonium system in 1977 is also summarized in Figure 1. The most distinctive evidence for the $\psi(3095)$ and $\psi'(3684)$ comes from their production in e^+e^- annihilation where they show up as huge peaks in the hadronic cross section. The other charmonium states below 3.7 GeV/c^2 have the wrong quantum numbers to be produced directly in e^+e^- annihilation. They are seen in radiative decays of the ψ and ψ'. Several methods have been used to observe these radiative decays.

1. Peaks in the inclusive energy distribution of photons from ψ' decays give strong evidence for the decay $\psi'\to\gamma\chi$ with χ masses of 3.415, 3.510, and 3.555 GeV/c^2.[3]

2. Strong evidence for states with these same 3 masses comes from observation of the decay $\psi'\to\gamma\chi$, $\chi\to$hadrons. These hadronic decays also provide information on the quantum numbers of the states.

---

[2]E. Eichten et al., Phys. Rev. D17, 3090 (1978); T. Appelquist et al., preprint SLAC-PUB-2100; V. A. Novikov et al., Phys. Reports 41C (1978); M Krammer and H. Krasemann, preprint DESY 79/20 (1979).

[3]C. J. Biddick et al., Phys. Rev. Lett. 38, 1324 (1977).

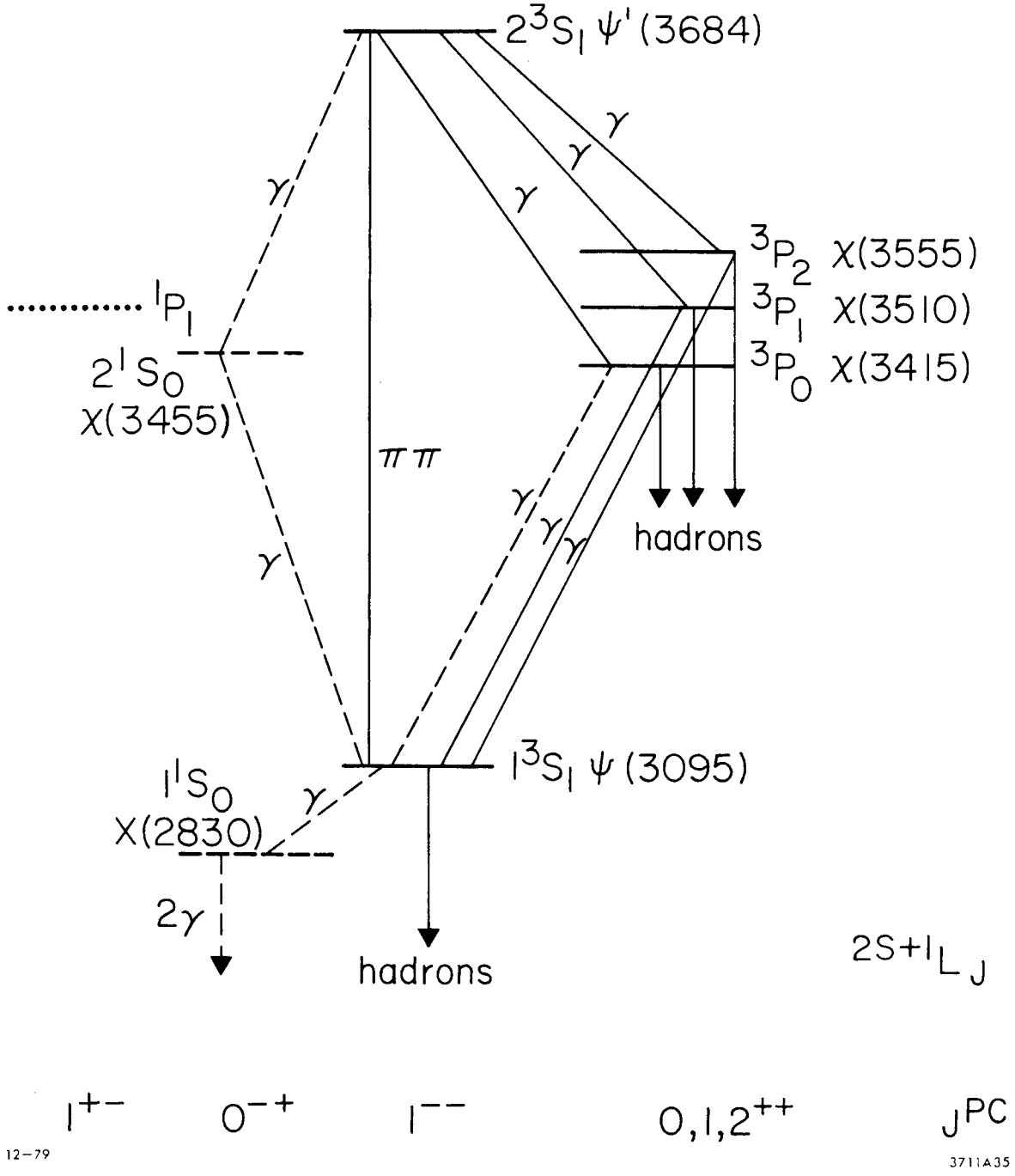

Figure 1: Charmonium level diagram: before. Solid lines indicate things confirmed by experiment. Dashed lines indicate things with a small amount of experimental evidence. Dotted lines indicate things predicted by the Charmonium model for which there is no experimental evidence.

3. The $\chi(3510)$ and $\chi(3555)$ have also been observed in the cascade decay $\psi' \to \gamma\chi$, $\chi \to \gamma\psi$.[4] In addition there is evidence for a fourth state, the $\chi(3455)$.[5] The evidence consists of 4 events where less than one event background was expected. This state has not been observed with any of the other methods. It is normally associated with the 2^1S_0 charmonium level, the η_c'. This association causes theoretical difficulties because calculations and measurements of its branching ratios differ by over an order of magnitude.

4. Evidence for the X(2830) came from the decay $\psi \to \gamma X$, $X \to \gamma\gamma$.[6] It has not been observed with any of the other methods. It is normally associated with the 1^1S_0 charmonium level, the η_c. Like the $\chi(3455)$, this association causes theoretical difficulties because calculations and measurements of its branching ratios differ by over an order of magnitude.

There are several excellent review papers[7] which summarize the experimental status of the charmonium system. Briefly, the $\psi(3095)$, $\psi'(3684)$, $\chi(3415)$, $\chi(3510)$, and $\chi(3555)$ states are well established. Enough of their quantum numbers have been measured so there is a unique

---

[4] W. Braunschweig et al., Phys. Lett. 57B, 407 (1975); W. Tanenbaum et al., Phys. Rev. D17, 1731 (1978).

[5] W. Tanenbaum et al., Phys. Rev. D17, 1731 (1978).

[6] W. Braunschweig et al., Phys Lett. 67B, 243 (1977).

[7] B. H. Wiik and G. Wolf, DESY 78/23 (1978); H. Schopper, DESY 77/79 (1977).

correspondence to the predicted charmonium levels. Evidence for the X(2830) and χ(3455) is much weaker and confirmation is needed.

To learn more about the charmonium system an experiment has been done with the SLAC-LBL Mark II magnetic detector at the e^+e^- storage ring, SPEAR. During 6 weeks of running, the decays of 10^6 ψ'(3684)'s have been observed. The general purpose Mark II detector combined with the high statistics data sample provides an excellent opportunity to study the charmonium system.

Chapter II

THE DETECTOR

The Mark II consists of a series of cylindrical detectors coaxial with the SPEAR beam line. There are drift chambers in a magnetic field to measure directions and momenta of charged particles, scintillation counters to measure their velocity, and shower counters to detect photons and identify electrons. An end view of the detector is shown in Figure 2.

A particle leaving the interaction region travels through the following parts of the detector.

1. The beam pipe is a cylinder of 0.21 mm thick corrugated stainless steel.

2. The pipe counter consists of two cylindrical, 0.6 cm thick, plastic scintillation counters. They are 81 cm long at radii of 11 and 12.5 cm. Each cylinder is divided in half along the vertical plane through the beam line.

3. The 16 drift chamber layers are at radii 0.414 m through 1.448 m with lengths of 1.984 m through 2.642 m. Six layers have axial wires (parallel to the beam line) and 10 layers have stereo angles of $\pm 3^0$ to provide position measurements in the axial direction. The resolution is typically σ=0.22 mm. More

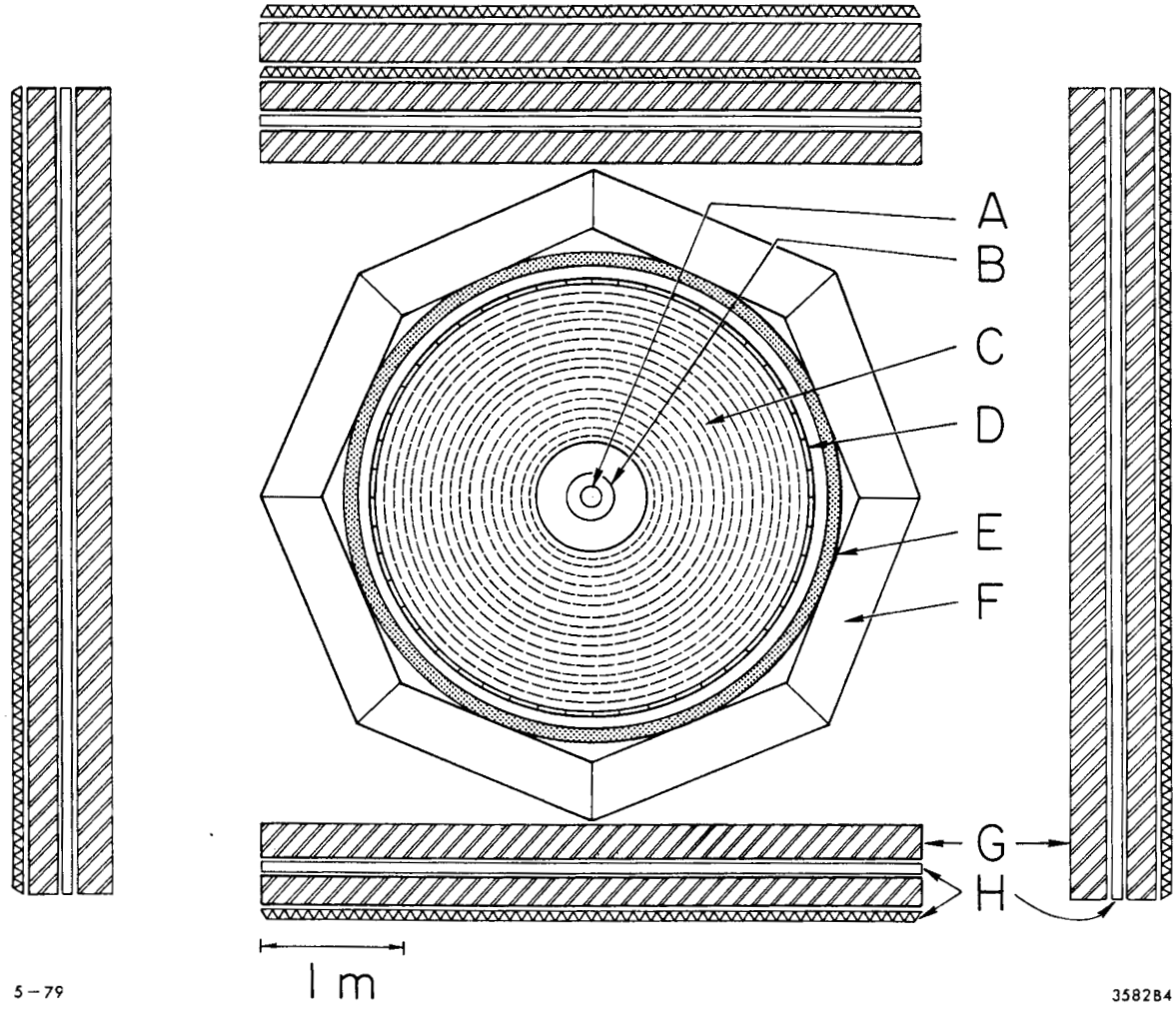

Figure 2: Schematic view of the Mark II detector.
(A) vacuum chamber, (B) pipe counter, (C) drift chamber, (D) time-of-flight counters, (E) solenoid coil, (F) liquid argon shower counters, (G) iron absorber, (H) muon proportional tubes.

information about the drift chamber is available in a previous publication.[8]

4. The 48 time-of-flight (TOF) counters are at radius 1.524 m with an active length of 3.442 m. They are viewed with XP2230 phototubes on both ends. The time-of-arrival and integrated charge of the phototube pulses are recorded.

5. The aluminum coil for the solenoid magnet contains most of the 1.6 radiation lengths of material which lies between the beam and the shower counter. The field was mapped with Hall and NMR probes before insertion of the drift chambers. A polynomial was fit to this field map with a maximum error of 0.03%. This fit is then used by the track reconstruction program. During data taking the magnetic field is monitored with an NMR probe. The systematic error in the field value is less than 0.2%.

6. The liquid argon shower counters form an octagon around the coil. Their active area subtends $0.64 \cdot 4\pi$ steradians. They contain 14 radiation lengths of lead and liquid argon. The lead is divided into strips with a width of 3.8 cm. These strips run parallel, perpendicular and at 45^0 to the beam direction to allow reconstruction of the shower position. More information about the shower counter is available in a previous publication.[9]

---

[8]W. Davies-White et al., Nucl. Instrum. Methods 160, 227 (1979).

[9]G. S. Abrams et al., IEEE Transactions on Nuclear Science NS-25, 309

7. The muon system subtends $0.5 \cdot 4\pi$ steradians. It consists of steel hadron filters (which double as the magnetic flux return) followed by proportional chamber tubes.

The ends of the cylinder are instrumented with shower counters. Each counter subtends $0.07 \cdot 4\pi$ str.

The trigger is described in minute detail in Appendix A. A brief description is given here. Both layers of the pipe counter must fire within ± 6 ns of the time the beams cross. This provides cosmic ray rejection. Then a track finding processor must find at least 2 tracks in the drift chambers, one of which must fire a TOF counter. The other need only go through the inside 5 drift chamber layers. All events satisfying these criteria are logged on tape.

(1978); G. S. Abrams et al., to be published in IEEE Transactions on Nuclear Science (1979) .

Chapter III

EVENT RECONSTRUCTION

The origin of the coordinate system used for the analysis is at the nominal beam collision point, the center of the detector. The x, y, and z axes point towards the center of SPEAR, up, and in the positron beam direction respectively. The polar angle, θ, is the angle between a vector and the +z axis. The azimuthal angle, ϕ, is the angle between the x axis and the projection of a vector on the x-y plane while r is the length of the projection of a vector on the x-y plane. The actual beam collision point, the interaction region, moves when the configuration of SPEAR is changed. This position is measured using Bhabha events ($e^+e^-\rightarrow e^+e^-$).

The event reconstruction starts with charged particle tracking. A pattern recognition program looks for hits in the drift chamber which lie on a helix. Since a helix has 5 free parameters, at least 5 measurements are needed to determine it. To provide redundancy and allow resolution of the right-left ambiguity the tracking program requires 7 hits on a track. This allows tracks with $|\cos\theta|<0.85$ to be found. The parameters of the track are obtained with a least squares fit to the measured drift times. The resolution of these drift time measurements was previously determined[10] and parameterized as a function of angle and

---

[10] W. Davies-White et al., Nucl. Inst. and Meth. 160, 227 (1979).

position in the drift cell. The fit uses these resolutions and the errors caused by multiple scattering to calculate an error matrix for the track.

Each track is projected to the time-of-flight counter radius. The z position where the track hit the counter and the times and pulseheights of the two phototube pulses are used to calculate a flight time. This time and the pathlength of the track determine the particle's speed. The speed and momentum can then be used for particle identification. Figure 3 shows the distribution of the expected time-of-flight minus the measured time-of-flight for muons in the decay $\psi' \to \pi^+\pi^-\psi$, $\psi \to \mu^+\mu^-$. The distribution is Gaussian with a standard deviation of 0.313 ns. This resolution provides 1σ e-π, π-K, K-p separation up to 0.3, 1.35, and 2.2 GeV, respectively.

To allow identification of electrons, the energy deposited in the liquid argon calorimeter by charged tracks is determined by summing the charge deposited on strips passing near the projection of the track.[11] The summed charge is converted to deposited energy using a calibration based on electro-magnetic shower Monte Carlo calculations,[12] and on measurements of Bhabhas and of photons from the decays $\psi \to \pi^+\pi^-\pi^0$ and $2\pi^+2\pi^-\pi^0$. Photons are detected in the calorimeter by looking for spacial coincidences of strips with deposited charge. Since liquid argon shower counters have no gas multiplication, very sensitive amplifiers

---

[11] G. S. Abrams et al., to be published in Nucl. Inst. and Meth.

[12] EGS Code, R. L. Ford and W. R. Nelson, SLAC Report No. 210 (1978).

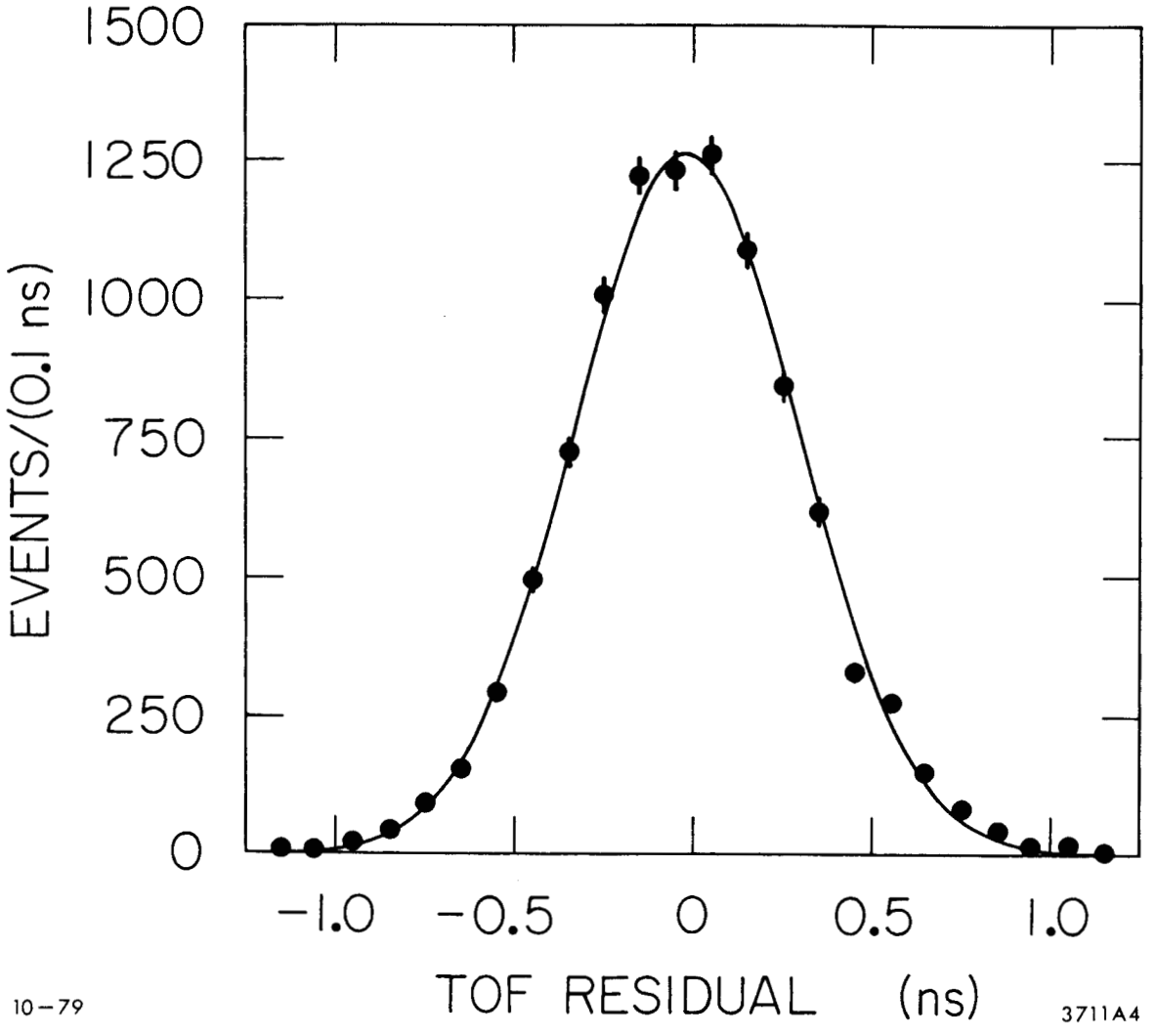

Figure 3: Time-of-flight resolution.
Expected TOF minus measured TOF for muons in the decay $\psi' \to \pi^+\pi^-\psi$; $\psi \to \mu^+\mu^-$.
The Gaussian fit has mean = -0.02 ns and sigma = 0.313 ns.

(capable of detecting 10 femtocoulombs) must be used. Thermal noise in the first stage of these amplifiers causes pulseheight to be recorded for strips which have no deposited charge. The pattern recognition program has pulseheight cuts to help prevent this noise from generating false photons. These cuts cause low efficiency for low energy photons. Figures 4 and 5 show the efficiency for photons and the energy spectrum of false photons. These properties are particularly important for this analysis. The angular resolution of the liquid argon system varies from 4 mrad for high energy tracks to 8 mrad for low energy tracks. The energy resolution is $\sigma=0.13\cdot\sqrt{E}$ (GeV).

The next step in the event reconstruction is vertex reconstruction. Charged particles can usually be identified as π's, K's or p's by TOF. The decays $K_s\rightarrow\pi^+\pi^-$ and $\Lambda\rightarrow\pi^-p$ are detected by looking for pairs of tracks consistent with such decays. Figure 6 shows the mass distribution for the candidate K_s's. After the mass cut indicated in the Figure, signal-to-noise is 0.81:1. For Λ's signal-to-noise is 5.1:1. From the remaining tracks, a primary vertex is found. If this has $R<4$ cm and $|z|<15$ cm, a beam constrained fit is done. Using the parameters and error matrices from the single track fits and the previously measured position and size of the beam, a vertex position is determined. By constraining the tracks to go through this vertex, one obtains beam constrained momenta and error matrices. The beam constrained fits have better resolution than the single track fits because the pathlength over which the track is measured is increased by >40%. The resulting momentum resolution is $\sigma^2/p^2 = .015^2+.005^2p^2$. This formula is calculated from the size of the beam spot and the drift chamber resolution (which causes the sec-

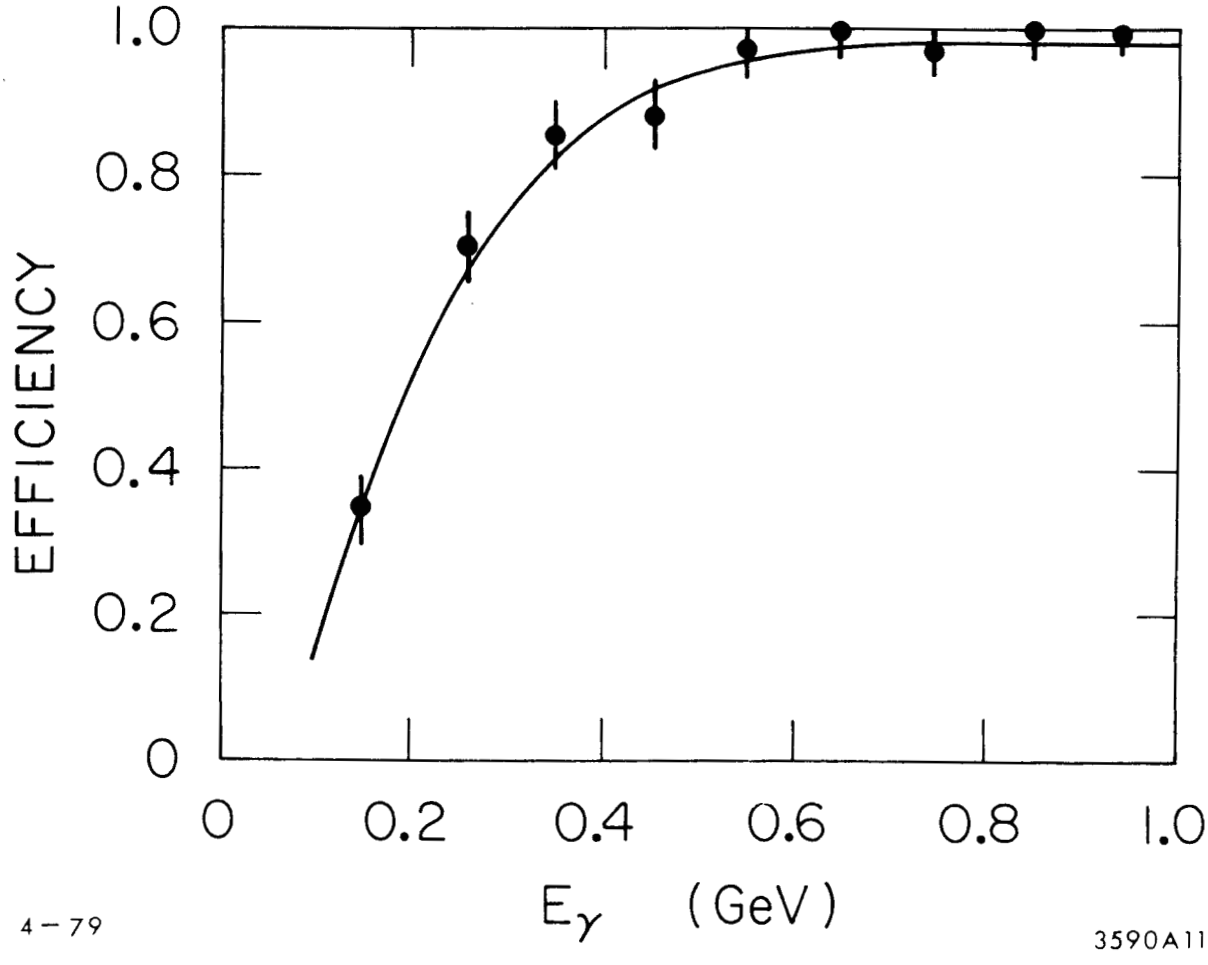

Figure 4: Photon efficiency.
The curve shows the efficiency found with the shower Monte Carlo. The points show the efficiency measured with $\psi \to \pi^+\pi^-\pi^0$ and $\psi \to 2\pi^+2\pi^-\pi^0$.

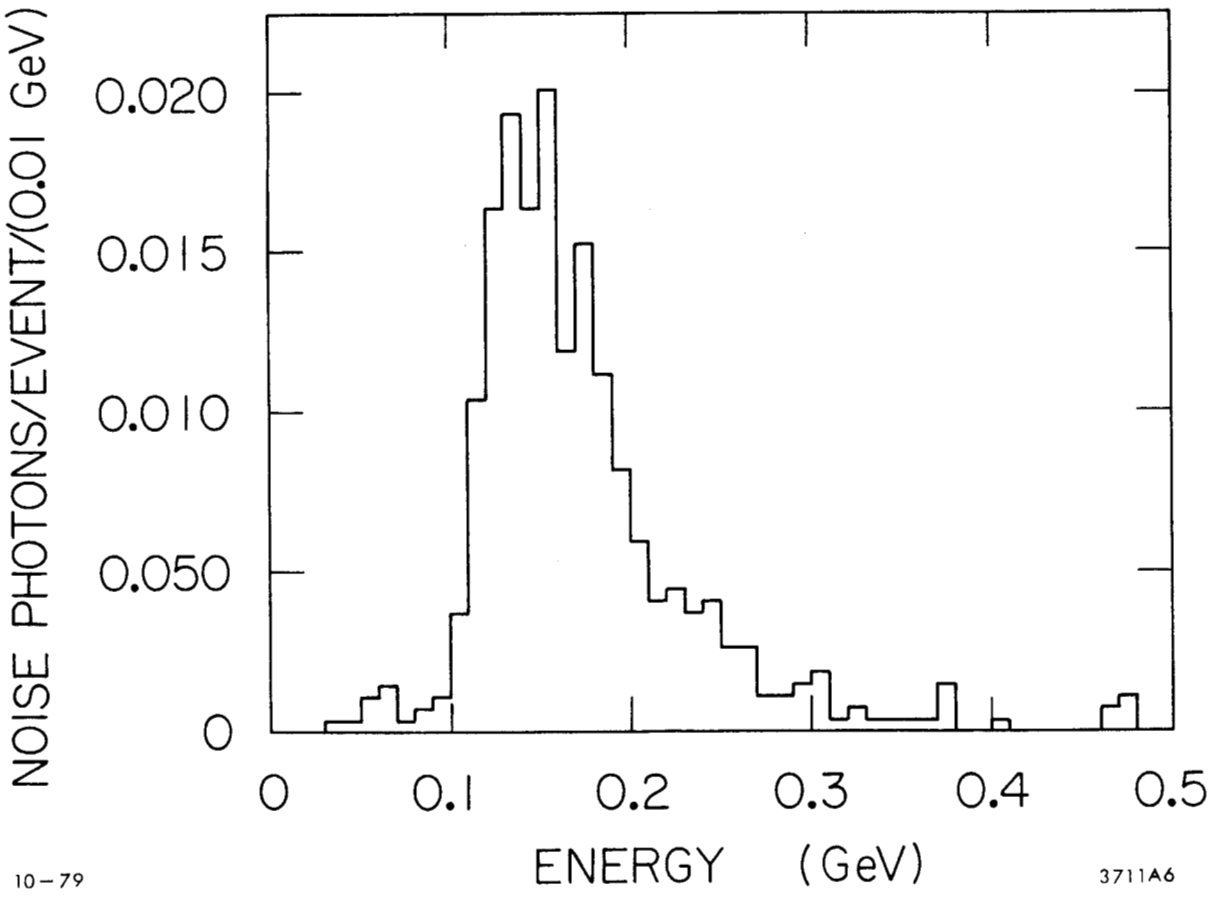

Figure 5: Liquid argon false photon spectrum.
Energy spectrum of photons found in $\psi' \to \pi^+\pi^-\psi$ events. There is an average of 0.2 false photons per event.

ond term) and multiple scattering (which causes the first term). The widths of the K_s and ψ peaks (Figures 6 and 7) agree with the expected resolutions. These data provide checks on the resolution both when it is multiple scattering limited and when it is limited by measurement error. The position of these peaks provides a check on the absolute scale of the momentum measurements. Our K_s mass measurement of 498.16±0.08 is 0.46 MeV/c^2 from the world average. The systematic error of .2% on the magnetic field can account for this difference. The ψ peak centers at 3096.2 MeV/c^2 which is 1.2 MeV/c^2 above the value determined by scanning SPEAR's energy over the peak. This difference is consistent with SPEAR's energy calibration error of 0.13%. In summary, both the resolution and the magnitude of the momentum are consistent with expected errors.

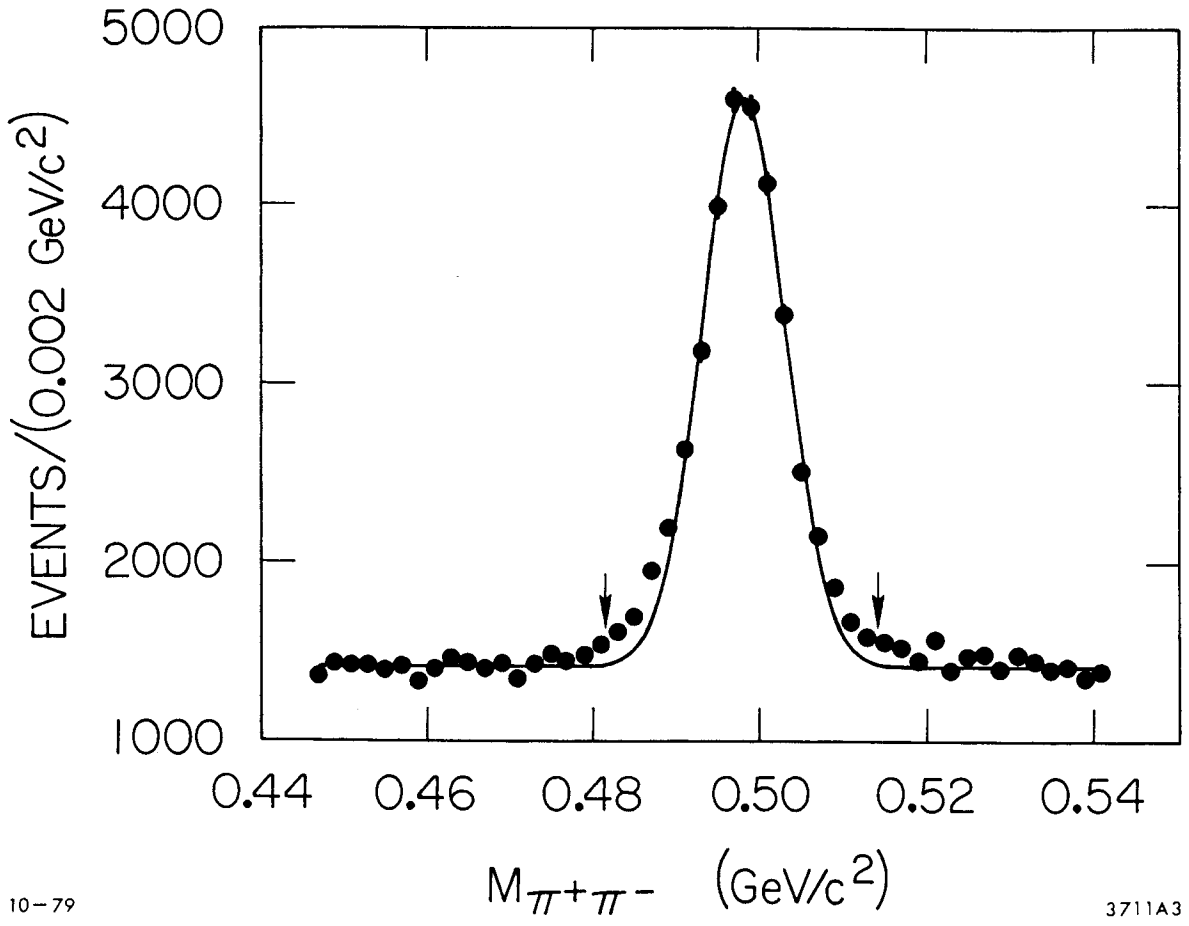

Figure 6: $\pi^+\pi^-$ mass of K_s decay candidates.
A fit to a Gaussian plus flat background gives mass and sigma of 498.16±0.08 and 5.0 MeV/c^2.

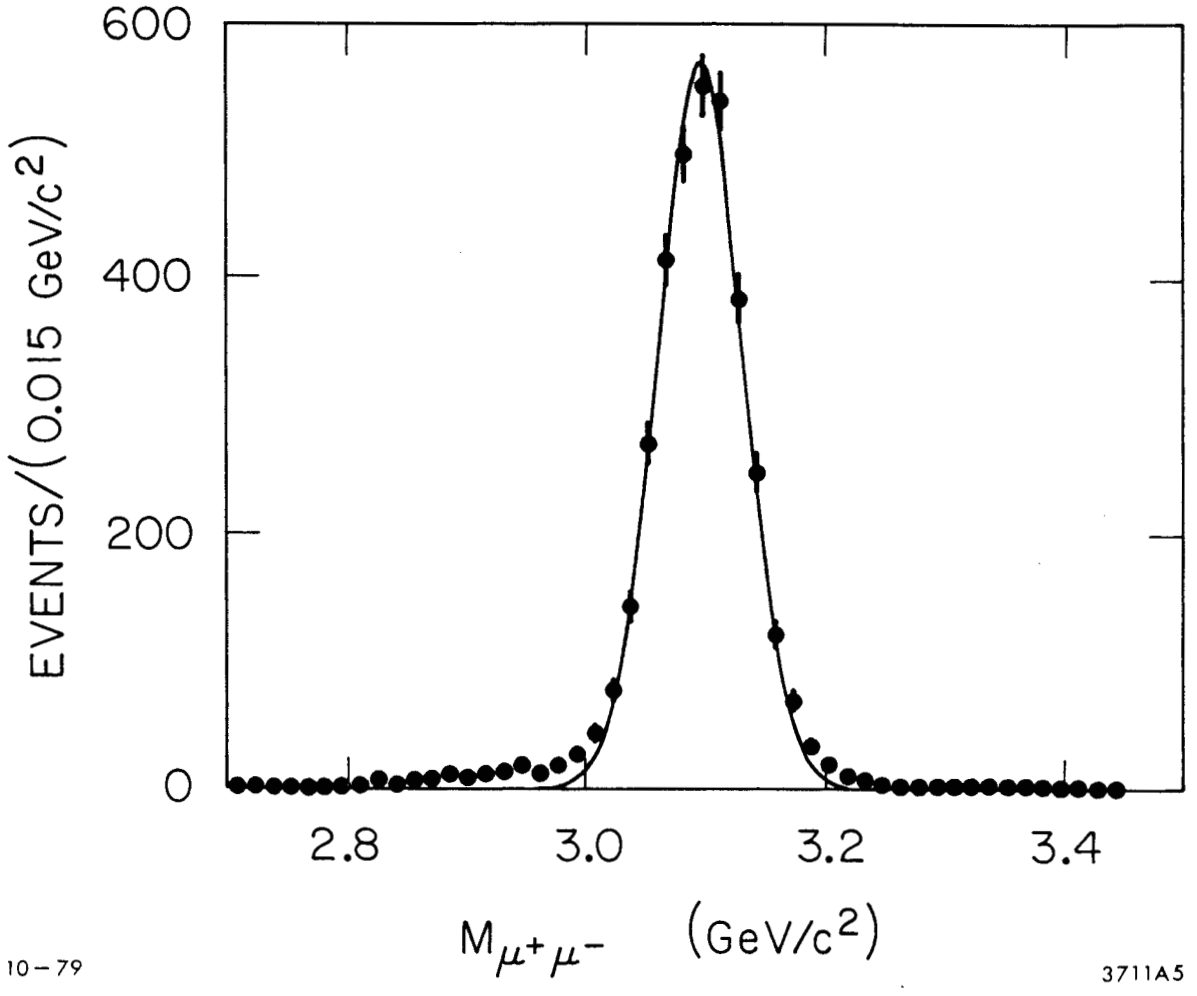

Figure 7: $\mu^+\mu^-$ mass of ψ decay candidates. A fit to a Gaussian plus flat background gives mass and sigma of 3096.2±0.7 and 35. MeV/c^2.

Chapter IV

$\psi' \to \pi^+\pi^-\psi$, $\psi \to \ell^+\ell^-$

The decay $\psi' \to \pi^+\pi^-\psi$, $\psi \to \ell^+\ell^-$ (ℓ=lepton) is interesting both for its physics implications and for its use as a tool in understanding the detector. The two high momentum leptons leave such a distinctive signature in the detector that one can get a nearly background free sample of events with very loose cuts. This allows comparison of the data with the Monte Carlo allowing checks that the resolution and acceptance of the detector are properly modeled by the Monte Carlo. The number of detected $\pi^+\pi^-\psi$ events gives the number of produced $\psi'(3684)$'s. The $\pi^+\pi^-$ mass distribution shows effects of the dynamics of this decay. Finally, the branching ratio for $\psi' \to \eta\psi$ can be measured from the decays $\eta \to \pi^+\pi^-\pi^0$ or $\pi^+\pi^-\gamma$.

4.1 THE MONTE CARLO

The Monte Carlo consists of two main parts: event generation and particle detection. The event generation is done with a simple phase space model. The decay sequence must be specified and the 3-momenta are distributed according to phase space. In some cases the phase space distribution has been modified to put in angular distributions caused by the dynamics of the interaction. This is explicitly mentioned wherever it is done.

To simulate particle detection, the generated particles are tracked through the detector and raw data (drift times, pulseheights...) are generated. These raw data are then analyzed by the same programs used for the real data. The following effects are included as part of the raw data generation.

1. The position of the primary vertex is distributed according to the known size of the beam.

2. The particles lose energy and undergo multiple coulomb scattering as they pass through material.

3. Photons can convert to e^+e^- pairs in the material through which they pass.

4. Electrons bremsstrahlung photons with the known energy spectrum.

5. Particles interact both elastically and inelastically with the nuclei in the material through which they pass. Measured cross sections are used.

6. Particles decay with their known lifetimes. This is especially important for charged K's, half of which decay before leaving the drift chamber.

7. The drift times in the drift chamber are generated with the measured resolution. This resolution varies with the position in the cell and the angle of the track.

8. The drift chamber cell efficiency is 95% to simulate the dead cells in the real drift chamber.

9. 1.5% of the drift times are generated with a random time between 0 and the expected drift time. This simulates an effect in the real data attributed to delta rays.

10. Two neighboring drift chamber cells sometimes fire, as observed in the real data.

11. Flight times to the TOF counters are generated with the measured resolution of 0.313 ns.

12. Raw data are not generated for the liquid argon system. The measured efficiency and resolution of the liquid argon system are used directly to generate the parameters of the photons which are found.

4.2 COMPARISON OF DATA AND MONTE CARLO

To compare data and Monte Carlo, we use $\psi' \to \pi^+\pi^-\psi$ events where one of the π's is allowed to be missing. From the 3 measured tracks and conservation of 4-momentum, the 4-momentum of the fourth track is calculated. Checking to see if the fourth track was detected gives the tracking efficiency as a function of 3-momentum. Repeating this for the data and the Monte Carlo with varying cuts on the fourth track provides a good check of the accuracy with which the Monte Carlo reproduces the data. It also allows one to estimate the systematic errors on branching ratios caused by uncertainties in the acceptance calculation. The Monte Carlo

events used for this comparison are generated with the $\pi^+\pi^-$ mass distribution observed in the data (Section 4.5.0) and the positive lepton is given a $1+\cos^2\theta$ distribution.

Figure 8 shows a typical $\pi^+\pi^-\psi$ event. Events with 3 or 4 detected charged tracks are used. Two of these must be of opposite charge with invariant mass within 0.1 GeV of the ψ mass. Both of these tracks must be identified as muons by the muon system or as electrons by the liquid argon system. To reduce background from events with a ψ and a converted photon, events are not used if there is a track of momentum < 1 GeV/c that is identified by TOF or liquid argon as an electron. To reduce problems caused by mismeasured tracks, each of the 3 tracks used in the following analysis must have $|z|$ at point of closest approach to the origin less than 0.1 m and radial distance of closest approach to the interaction region less than 0.005/p (m/Gev).

For these events, the sum of the 4-momenta of the two leptons is constrained to give the ψ mass. This improves the resolution. Figure 9 shows the distribution of the mass squared (M^2) recoiling against the $\pi\psi$. Events with 2π's satisfying the above cuts appear twice in this histogram. The peak comes from $\psi'\rightarrow\pi^+\pi^-\psi$. It will be shown below that the shoulder at high recoil mass comes from $\psi'\rightarrow\eta\psi$, $\eta\rightarrow\pi^+\pi^-\pi^0$ or $\pi^+\pi^-\gamma$. To select the $\pi^+\pi^-\psi$ events we require $0.0<M^2<0.035$. The following analysis has also been done with much looser cuts, giving consistent results. This, together with the results of scanning several hundred event pictures, indicates that less than 1% of the events are background.

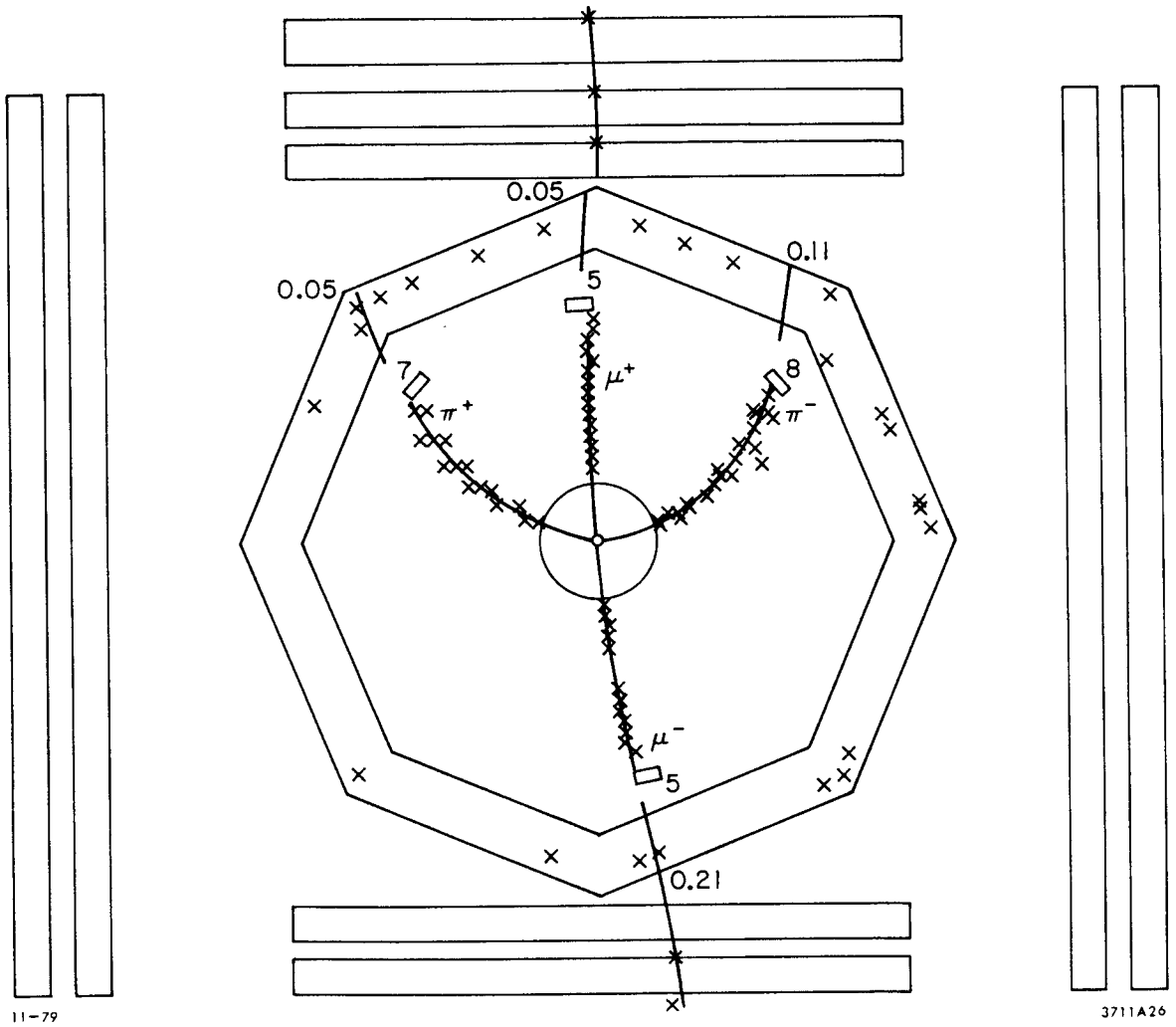

Figure 8: Typical $\pi^+\pi^-\psi$ event.
The numbers just outside the octagon are liquid argon pulseheights in GeV. The numbers by the small rectangles (representing the TOF counters) are the measured flight times in ns.

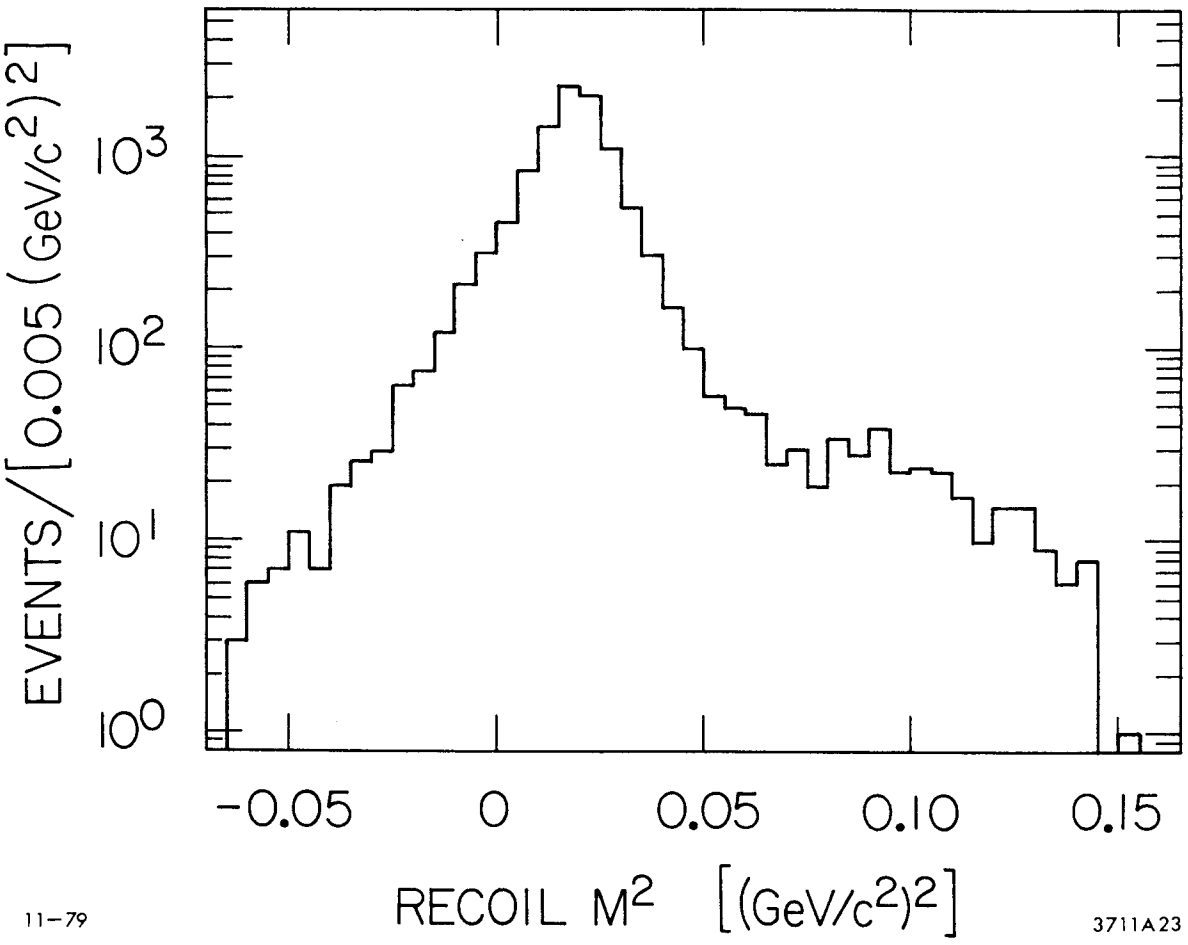

Figure 9: Mass squared recoiling against the $\pi\psi$

For each set of 3 tracks which satisfy the above cuts, the 3-momentum of the fourth is calculated. The average errors on this prediction are $\pm 7^0$ in angle and ± 0.021 GeV/c in p_t (momentum transverse to the beam direction). Checking to see how often the fourth track is found and satisfies various quality cuts gives the efficiency as a function of these cuts. The variables used are r_0 = r at point of closest approach of the track to the origin; $z_0 = |z|$ at point of closest approach to the origin; and r_{00} = radial distance from the track to the interaction region. Table 1 compares the efficiencies obtained from the data and the Monte Carlo with various cuts. These efficiencies are for tracks with predicted $|\cos\theta| < 0.5$ and $p_t > 0.1$ GeV/c. The inefficiency is caused by particle decays, nuclear interactions in the pipe counter, and pattern recognition problems. Figure 10 compares the efficiencies as a function of p_t. Note that these curves actually show the true efficiency smeared out by the resolution of 0.021 GeV/c. Since the efficiency drops sharply for $p_t < 0.1$ GeV/c, such tracks will not be used in later analysis. Similarly, the efficiency drops sharply for $|\cos\theta| > 0.76$, (the Monte Carlo and data disagree by 0.02 on the location of this drop) so such tracks will not be used in later analysis. Figure 11 compares the r_0 distributions. The non-Gaussian tails are primarily due to particle decays and nuclear interactions. Since the tails differ slightly between data and Monte Carlo, the r_0 cut used in later analysis will be 0.06 m. This minimizes systematic errors due to the different tails. Similarly, the cut $z_0 < 0.15$ m will be used. Table 1 shows that for these cuts the Monte Carlo and data efficiencies differ by $(0.3 \pm 0.6)\%$. In acceptance calculations a systematic error of 1.0% times

the number of charged tracks is used to allow for this uncertainty in the efficiency.

TABLE 1

Comparison of tracking efficiencies

Quality cuts	Data Efficiency (%)	Monte Carlo Efficiency (%)
none	95.6±0.3	94.2±0.3
$r_0<0.06$	92.5±0.4	92.3±0.4
$r_0<0.06$, $z_0<0.15$	90.5±0.4	90.2±0.4
$r_{00}<0.015$, $z_0<0.15$	81.9±0.6	80.2±0.5

The muons from $\pi^+\pi^-\psi$ events are used to check the TOF system. The TOF residuals are shown in Figure 3. The measured resolution of 0.313 ns is used in the Monte Carlo. The measured efficiency of 98.8% is not in the Monte Carlo, but we correct for it in later acceptance calculations. Similarly, we correct for the effect of the small non-Gaussian tails (1.6% of the events are outside 2.6σ rather than the expected 1%). Uncertainties in these corrections contribute a systematic error of 1% times the number of tracks for which TOF is required. This error and that due to the charged track detection efficiency will be added in quadrature to give the systematic error in later acceptance calculations.

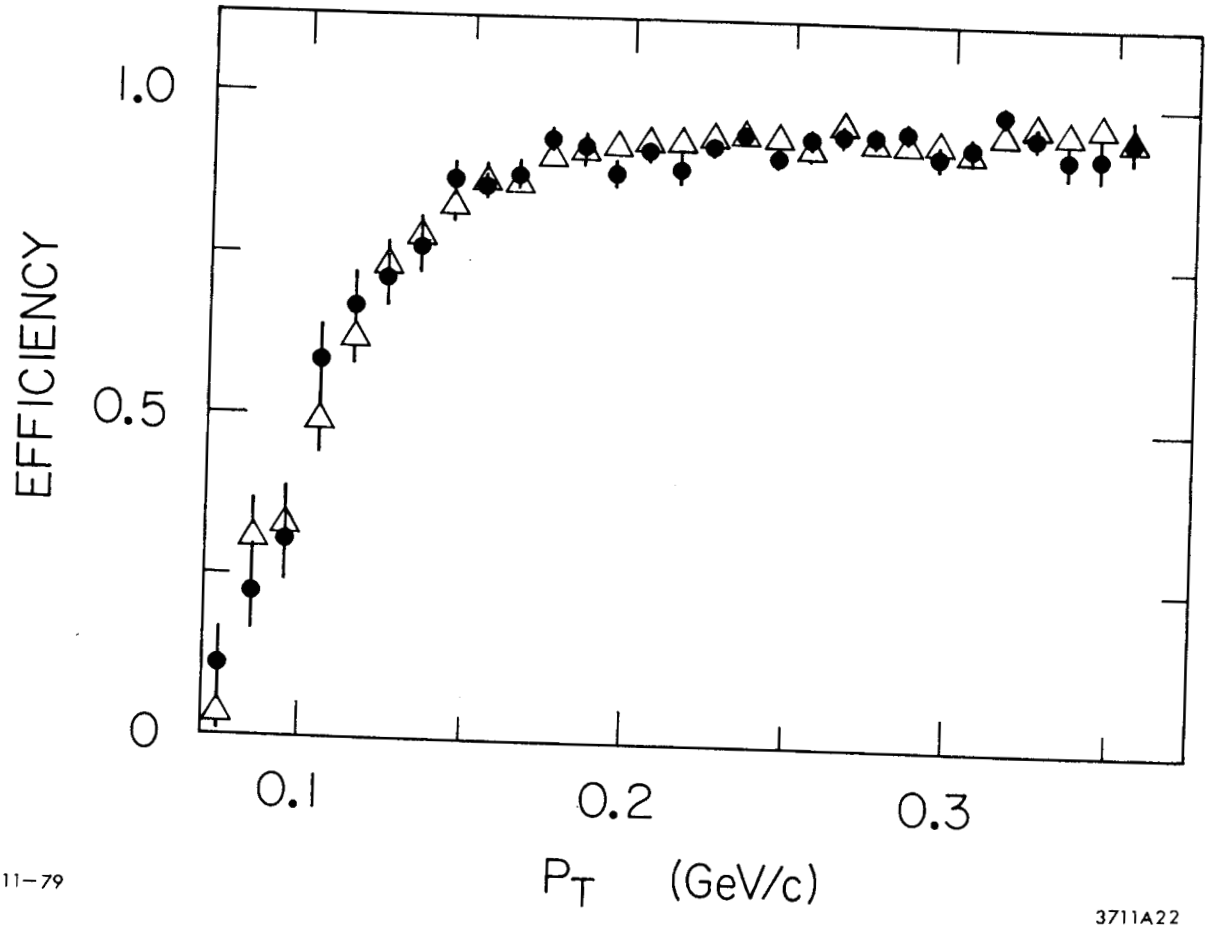

Figure 10: Tracking efficiency vs. p_t.
The solid points are data and the open triangles are Monte Carlo. Tracks must have $r_0<0.06$ m and $|z|<0.16$ m to be counted as efficient.

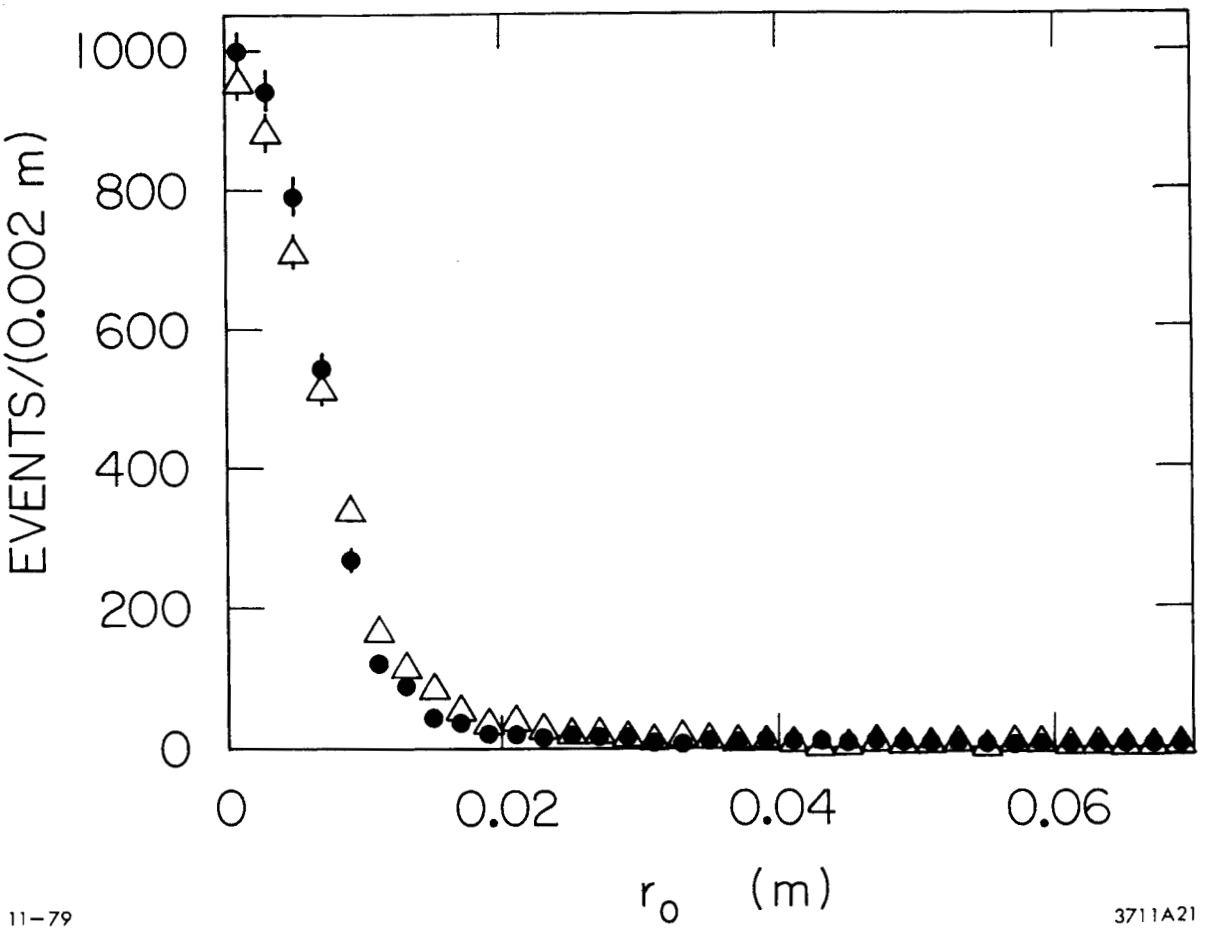

Figure 11: Comparison of r_0 distributions.
The solid points are data and the open triangles are Monte Carlo.

4.3 $\psi' \to \eta\psi$, $\eta \to \pi^+\pi^-\pi^0$ OR $\pi^+\pi^-\gamma$

Following the method used by the Mark I group,[13] we now investigate $\psi' \to \eta\psi$. The cuts used in this analysis are the same as those in the previous section up to the cut on the mass squared recoiling against the $\pi\psi$. The events where this recoil mass is large (Figure 9) arise from the decay $\psi' \to \eta\psi$. This is seen in Figure 12 where the M^2 recoiling against the ψ is plotted separately for events with M^2 recoiling against the $\pi\psi$ greater than 0.08 and between 0.0 and 0.035 $(GeV/c)^2$. The first group of events has a peak of 251 events at the η mass with width consistent with our resolution. The second group has a much broader mass spectrum. The background under the η peak from $\psi' \to \pi^+\pi^-\psi$ is calculated in two ways: by Monte Carlo and by assuming the peak in Figure 9 is symmetric about the π mass. They give 21 and 52 events, respectively; the average is used for the background subtraction. The Monte Carlo predicts no background from $\psi' \to \gamma\gamma\psi$ or $\psi' \to \pi^0\pi^0\psi$ where a γ converts. The acceptance for $\psi' \to \eta\psi$ is also obtained by Monte Carlo where the η is produced with a $1+\cos^2\theta$ distribution. Using the number of produced $\psi'(3684)$'s which will be calculated in the next section, the branching ratio for $\psi' \to \eta\psi$ is $(3.0 \pm 0.5)\%$. The error includes the statistical and systematic error on the number of produced η's and the systematic error on the number of produced $\psi'(3684)$'s.

---

[13] W. Tanenbaum *et al.*, Phys. Rev Lett. 36, 402 (1976).

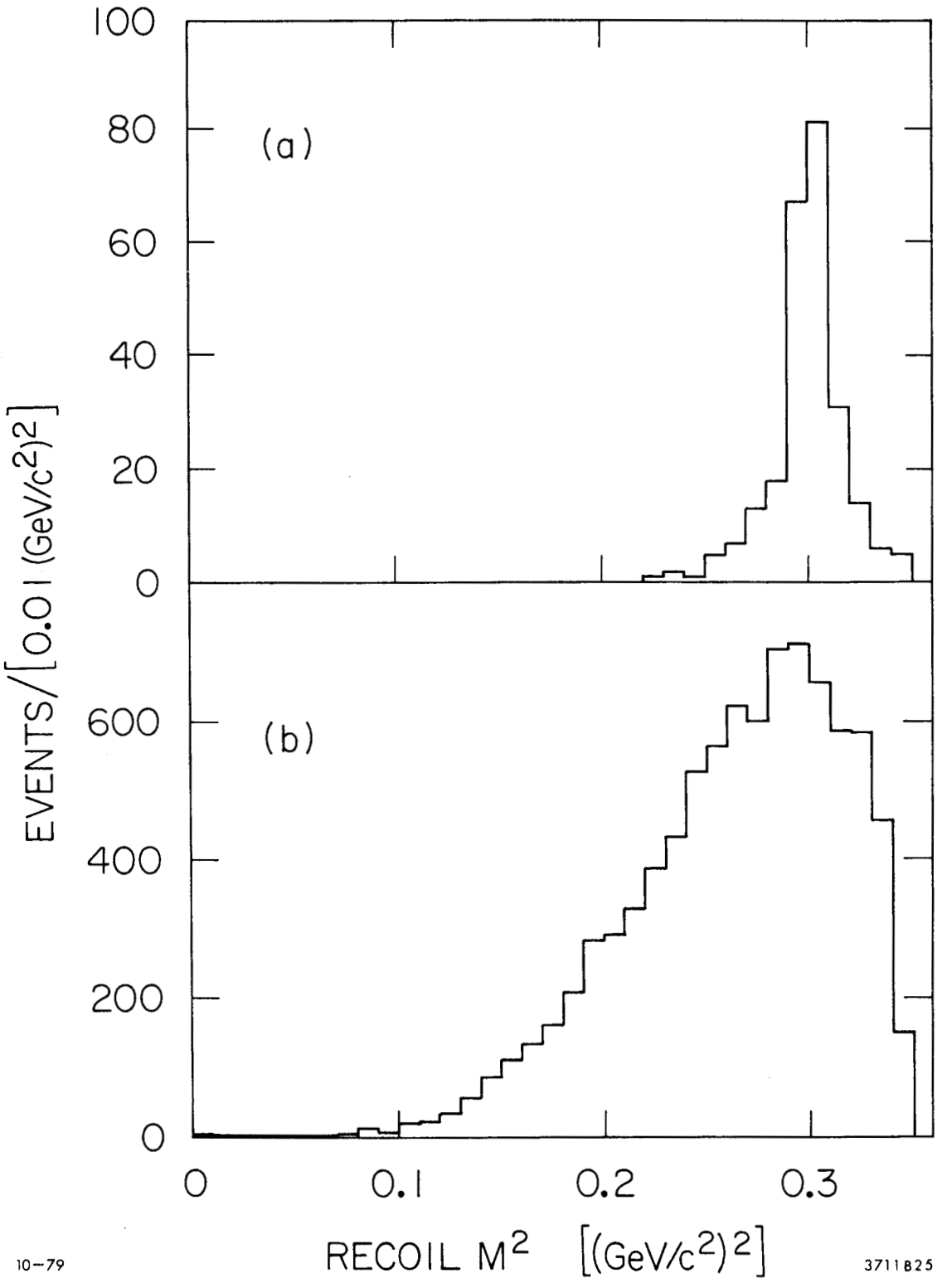

Figure 12: M^2 recoiling against the ψ.
for (a) M^2 recoiling against the $\pi\psi$ greater than 0.08; for (b) M^2 recoiling against the $\pi\psi$ between 0 and 0.035.

4.4 NUMBER OF PRODUCED $\psi'(3684)$'S

By counting the number of detected $\psi' \to \pi^+\pi^-\psi$, $\psi \to \ell^+\ell^-$ events and using previously measured branching ratios for $\psi' \to \pi^+\pi^-\psi$ and $\psi \to \ell^+\ell^-$, the number of $\psi'(3684)$'s produced in this experiment can be calculated. This number will then be used to calculate branching ratios for other reactions.

To do this we will count the total number of 4 prong events which contain a ψ decay to leptons and subtract the number of these which result from $\psi' \to \eta\psi$, $\eta \to \pi^+\pi^-\pi^0$ or $\pi^+\pi^-\gamma$. Events are selected by requiring exactly 4 charged tracks to pass within $r < 0.06$ m and $|z| < 0.15$ m from the origin. These four tracks must have $|\cos\theta| < 0.76$ and $p_t > 0.1$ GeV/c. The total charge must be zero. To eliminate events with converted photons, events with two tracks of opposite charge with cosine of the angle between them greater than 0.95 are removed. For the remaining events Figure 13 shows a histogram of the largest invariant mass of a neutral particle pair. For this purpose, the events were divided into 3 classes: both particles of the high mass pair are identified as electrons by the liquid argon system, both particles are identified as not being electrons by the liquid argon system, and other (e.g. a particle missed the active liquid argon volume). All 3 classes are used in counting the total number of events; the separation is only used to compare $\psi \to e^+e^-$ and $\psi \to \mu^+\mu^-$. The low mass tail in the "e^+e^-" spectrum is primarily caused by radiation of the electrons. A check of events in the low mass tail of the "$\mu^+\mu^-$" mass spectrum shows that half of them are really $\mu^+\mu^-$ events (identified by the muon system) and the other half are not muons (they are probably π's or K's). Since the ψ signal is so clean,

the last cut needed is to require this particle pair mass to be between 2.8 and 3.4 Gev/c^2. 10221 events satisfy this cut. From the low mass tail of the "$\mu^+\mu^-$" spectrum, 110±50 of these events do not really contain a ψ decay. An additional subtraction of 70±30 events is made to remove events of the form $\psi' \to \eta\pi$, $\eta \to \pi^+\pi^-\pi^0$ or $\eta \to \pi^+\pi^-\gamma$. This results in 10041±117 detected $\psi' \to \pi^+\pi^-\psi$, $\psi \to \ell^+\ell^-$ events.

The detection efficiency is calculated by Monte Carlo. Phase space is modified by throwing the $\pi^+\pi^-$ mass according to the distribution in the next section. The positive lepton is forced to have a $(1+\cos^2\theta)$ angular distribution. Finally, the leptons from the ψ decay can radiate internally (immediately after leaving the vertex). Since 38% of the $\psi \to e^+e^-$ events are lost due to radiation causing the e^+e^- mass to be less than 2.8 GeV/c^2, it is important to check that the Monte Carlo properly models this radiation. Assuming that the branching ratios for $\psi \to e^+e^-$ and $\psi \to \mu^+\mu^-$ are equal, the data and Monte Carlo agree on the following ratios: (number of detected $\mu^+\mu^-$)/(number of detected e^+e^-), fraction of the total e^+e^- events in the tail between 2.8 and 2.975 GeV/c^2, and fraction of the total $\mu^+\mu^-$ events in the tail between 2.8 and 2.975 Gev/c^2. Since the radiative tails seem to be properly modeled, the systematic error on the acceptance is just 4% as calculated in section 4.2.0 . Thus there are 47,150±1900 $\psi' \to \pi^+\pi^-\psi$, $\psi \to \ell^+\ell^-$ events produced. Using previously measured branching ratios[14] for $\psi' \to \pi^+\pi^-\psi$ (0.33±.03) and $\psi \to \ell^+\ell^-$ (0.14±.02) gives $(1.02\pm0.04\pm0.17)\cdot10^6$ $\psi'(3684)$'s produced for this experiment. The first error is from the acceptance calculation.

---

[14] Particle Data Group, Phys. Lett. 75B (1978).

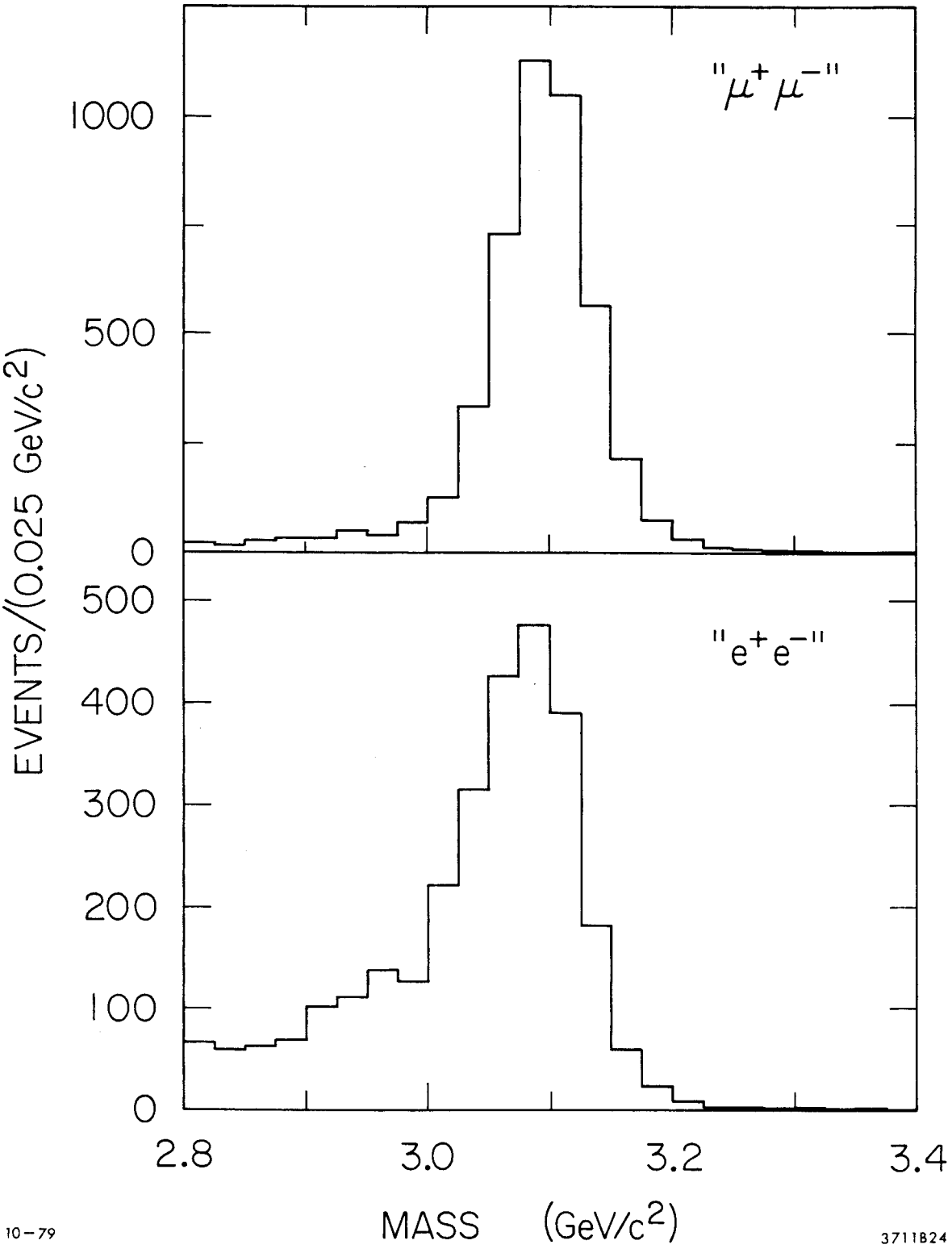

Figure 13: Mass of charge 0 pair in 4 prong events

The second error is from the errors on the previously measured branching ratios. This number of produced $\psi'(3684)$'s will be used below to calculate branching ratios.

4.5 DYNAMICS OF THE DECAY $\psi' \to \pi^+\pi^-\psi$, $\psi \to \ell^+\ell^-$

The decay $\psi' \to \pi^+\pi^-\psi$ is a good place to study the $\pi^+\pi^-$ interaction. Photoproduction experiments[15] indicate that the ψ nucleon interaction is much weaker than the π nucleon interaction. So the dynamical structure of the $\psi' \to \pi^+\pi^-\psi$ decay is primarily determined by the final-state interaction of the outgoing pions. Since both ψ and ψ' have isospin zero, the dipion system must also have I=0. Previous studies of angular distributions[16] show that the $\pi^+\pi^-$ usually have zero relative orbital angular momentum. Studies of our data (to be published) indicate that the D-wave amplitude is less than 10%.

To study this system we use those events from the previous section which have a mass recoiling against the $\pi^+\pi^-$ system between 3.06 and 3.13 GeV/c^2. This helps ensure that the π's are well measured. The $\pi^+\pi^-$ mass distribution of the 9248 remaining events is shown in Figure 14a. Figure 14b shows the mass distribution for the s-wave phase space Monte Carlo. The different forms of these two spectra show that final state interactions are important. The square root of the quotient of the two above distributions is shown in Figure 14c.

---

[15] U. Camerini *et al.*, Phys. Rev. Lett. 38, 263 (1977).

[16] G. S. Abrams, Proceedings of the 1975 Symposium on Lepton and Photon Interactions at High Energies, 25.

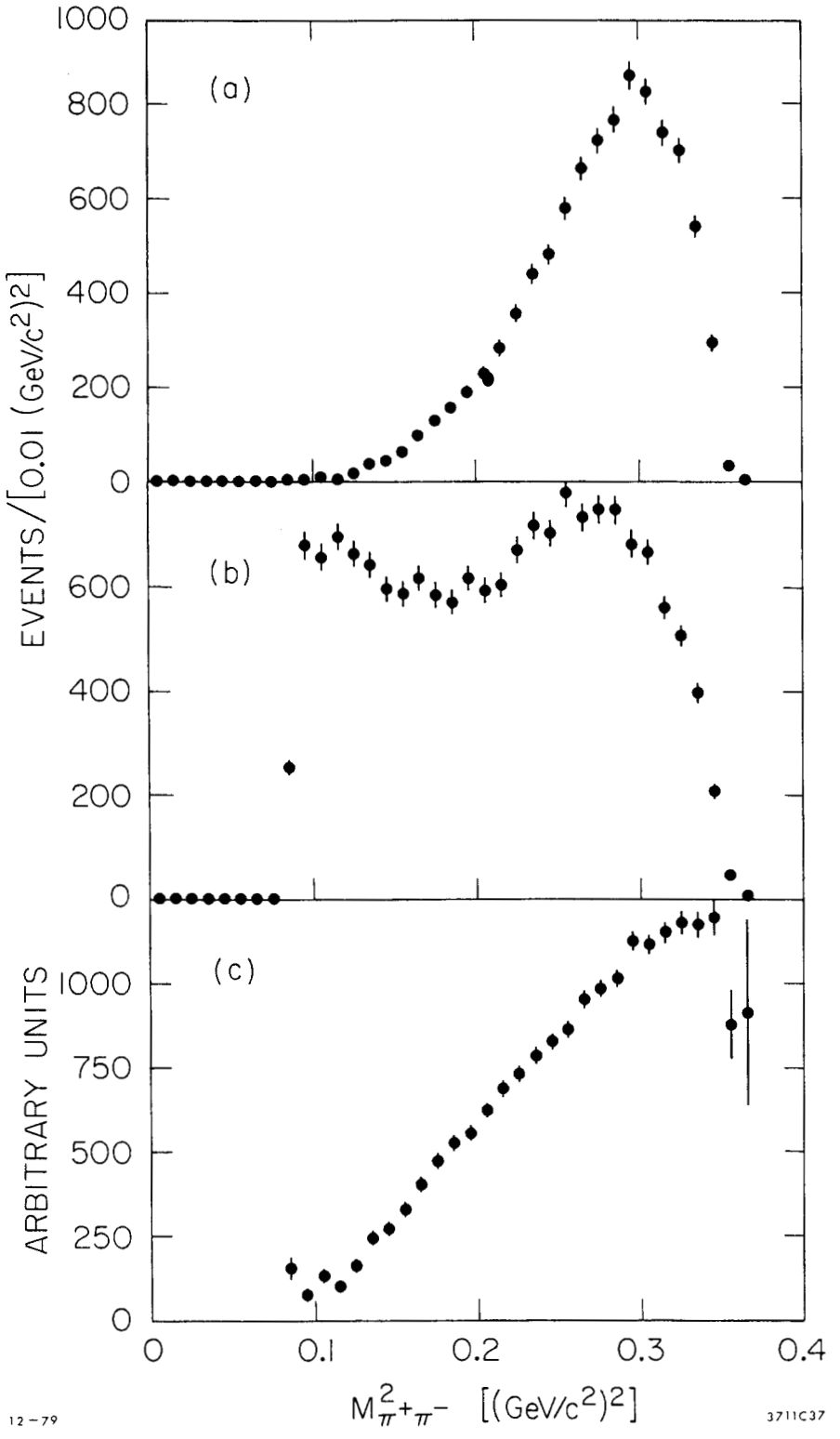

Figure 14: $\pi^+\pi^-$ mass distribution.
(a) the data; (b) the phase space Monte Carlo; (c) the square root of (a)/(b).

Since the $\pi^+\pi^-$ system is dominantly s-wave, Figure 14c gives the magnitude of the s-wave matrix element. The shape of this curve can be directly compared to theoretical predictions. Note that the normalization is arbitrary, and thus only the shape has any physical significance.

The 4 points at lowest mass should be ignored because there are so few signal events in these bins that the background events become important. The 4 points at highest mass should be ignored because the phase space factor changes very rapidly there and the Monte Carlo may not properly simulate the data in this respect.

Since the original measurement of the $\pi^+\pi^-$ mass spectrum, explanations have been published in several papers. Methods used include an intermediate ϵ resonance[17] and partially conserved axial-vector currents.[18] Both methods predict a straight line for the matrix element, but more work is needed to properly calculate the x-intercept of the line.

---

[17]R. Decker and M. Moreno, Nuo. Cim. Lett. 13, 407 (1975); B. J. Harrington, S. Y. Park, and A. Yildiz, Phys. Rev. D12, 2765 (1975).

[18]L. S. Brown and R. N. Cahn, Phys. Rev. Lett. 35, 1 (1975); D. Morgan and M. R. Pennington, Phys. Rev. D12, 1283 (1975).

Chapter V

$\psi' \to \gamma\gamma\psi$

The decay $\psi' \to \gamma\gamma\psi$ has been observed by several experiments.[19] This final state can result from the decays

1. $\psi' \to \eta\psi$, $\eta \to \gamma\gamma$

2. $\psi' \to \gamma\chi$, $\chi \to \gamma\psi$

3. $\psi' \to \pi^0\psi$, $\pi^0 \to \gamma\gamma$.

The last decay mode violates isospin conservation and has only recently been observed.

5.1 EVENT SELECTION

A typical event of the topology we are looking for is shown in Figure 15. We require that at least two photons be detected in the barrel liquid argon calorimeter. Photons detected within 0.3 m. of a charged track are not used. This helps eliminate false photons caused by energy deposited by the charged track. It also helps eliminate photons radiated by the outgoing electrons. Events with more than two detected photons are included in the sample because noise in the liquid argon pream-

---

[19] W. Tanenbaum et al., Phys. Rev. D 17, 1731 (1978); W. Bartel et al., Phys. Lett. 79B, 492 (1978); R. Brandelik et al., DESY 79/31 (1979).

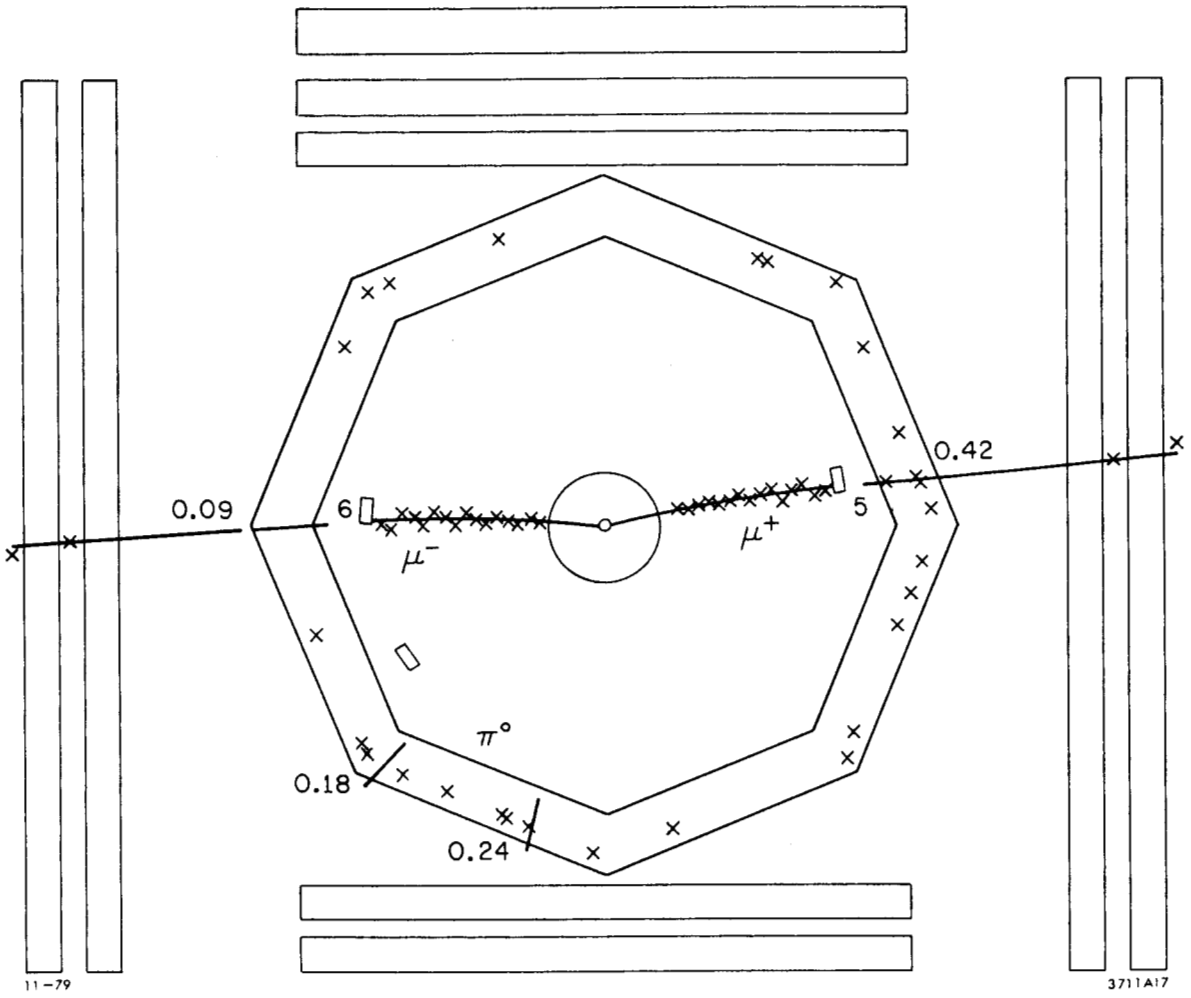

Figure 15: A $\psi' \to \pi^0 \psi$ event.

plifiers sometimes causes the tracking programs to find a false photon. The losses, if such events were eliminated, would be difficult to calculate precisely.

In those events with at least two photons, the ψ is detected by its decay to two leptons: $\psi \to e^+e^-$ or $\psi \to \mu^+\mu^-$. We require that there be exactly one positive and one negative particle coming from the interaction region, that is, they must have $r < 0.06$ m. and $|z| < 0.15$ m. at their point of closest approach to the origin. Figure 16 shows the mass distribution of these particle pairs. The peak at 3.095 GeV/c^2 is from the decay $\psi \to 2$ leptons. The shaded region shows only those events where both particles are identified by the liquid argon system as not being electrons. The low mass tail of the unshaded region comes from $\psi \to e^+e^-$ where an electron radiates a photon. The high mass tail comes from $e^+e^- \to e^+e^-$ where an electron radiates. The selection of $\psi(3095)$'s is made by requiring the dilepton mass to be between 2.8 and 3.4 GeV/c^2.

Events satisfying these cuts are fit to the hypothesis $\psi' \to \gamma\gamma\psi$, $\psi \to \ell^+\ell^-$ with the kinematic fitting program SQUAW. In events with more than two photons, fits are attempted with each photon pair. Generally only one such fit succeeds. This fit greatly improves the mass resolution which otherwise is limited by the energy resolution of the liquid argon calorimeter. Figure 17 shows the χ^2 probability distribution for this 5-constraint fit. The peak at low probability indicates a background contamination. To reduce background, the χ^2 probability is required to be more than 0.08. Most of this background comes from $\psi' \to \pi^0\pi^0\psi$. The smooth curve in the following mass plots is a Monte Carlo calculation of

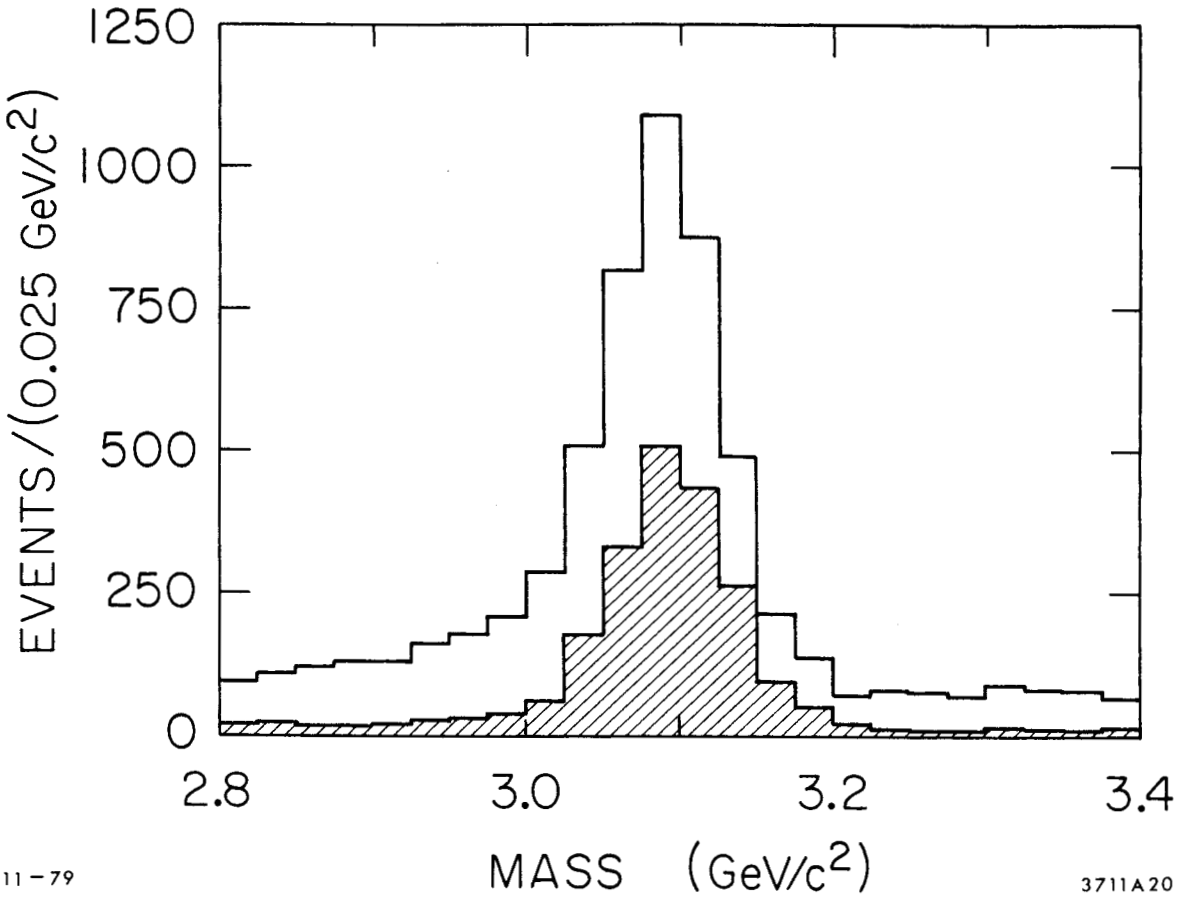

Figure 16: Mass of plus-minus particle pair.
Shaded region contains events where particles are not electrons.

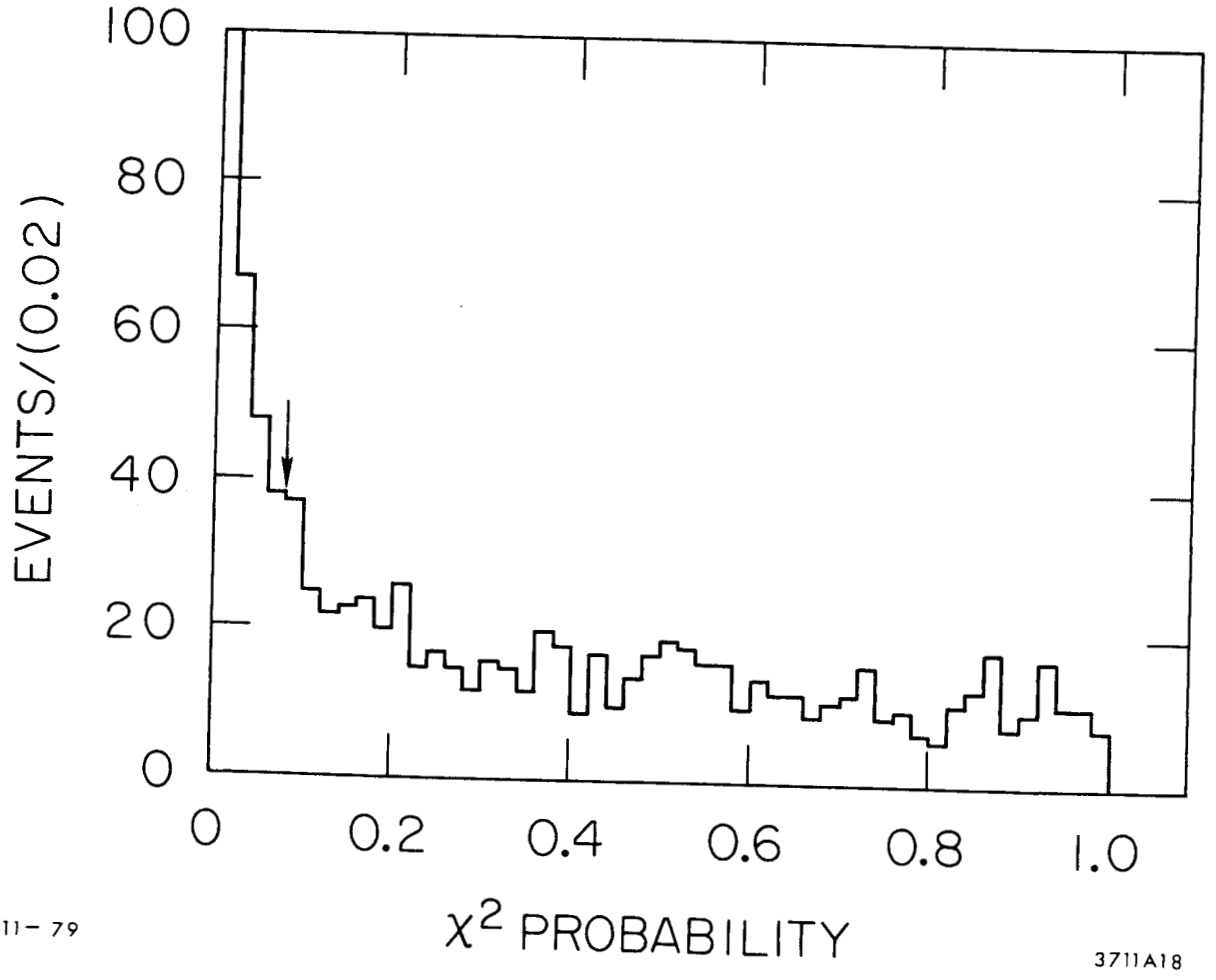

Figure 17: χ^2 probability distribution for 5C fit $\psi' \to \gamma\gamma\psi$, $\psi \to \ell^+\ell^-$.

this background. The Monte Carlo was run with the same parameters used for generating $\pi^+\pi^-$ events in section 4.5.0 .

5.2 $\psi'\to\eta\psi$

Figure 18 shows the $\gamma\gamma$ mass spectrum of the remaining events. The sharp peak at 547.56±0.17 MeV/c^2 comes from $\psi'\to\eta\psi$, $\eta\to\gamma\gamma$. The width of this peak is consistent with the expected mass resolution of ±1.7 MeV/c^2. The error given for the central value of the peak is statistical only. There is an additional systematic error of 0.0008 GeV/c^2 due to the uncertainty of the ψ'-ψ mass difference. The consistency of this mass with the accepted value provides a check on the systematic errors.

The background in Figure 18 comes from two sources: $\psi'\to\pi^0\pi^0\psi$ and $\psi'\to\gamma\chi$, $\chi\to\gamma\psi$. The smooth curve in the Figure is the Monte Carlo calculation of the first source. Note that it peaks at high mass as the $\pi^+\pi^-$ mass in $\psi'\to\pi^+\pi^-\psi$ does (section 4.5.0). Estimating the background from the 6 bins on each side of the η peak, there are 166±14 signal events. The acceptance (including branching ratios for $\eta\to\gamma\gamma$ and $\psi\to\ell^+\ell^-$) is (0.66±0.13)%. The systematic error is primarily due to uncertainty in the photon detection efficiency. The number of produced ψ'(3684)'s from section 4.4.0 then gives the branching ratio $\psi'\to\eta\psi$ = (2.5±0.6)%.

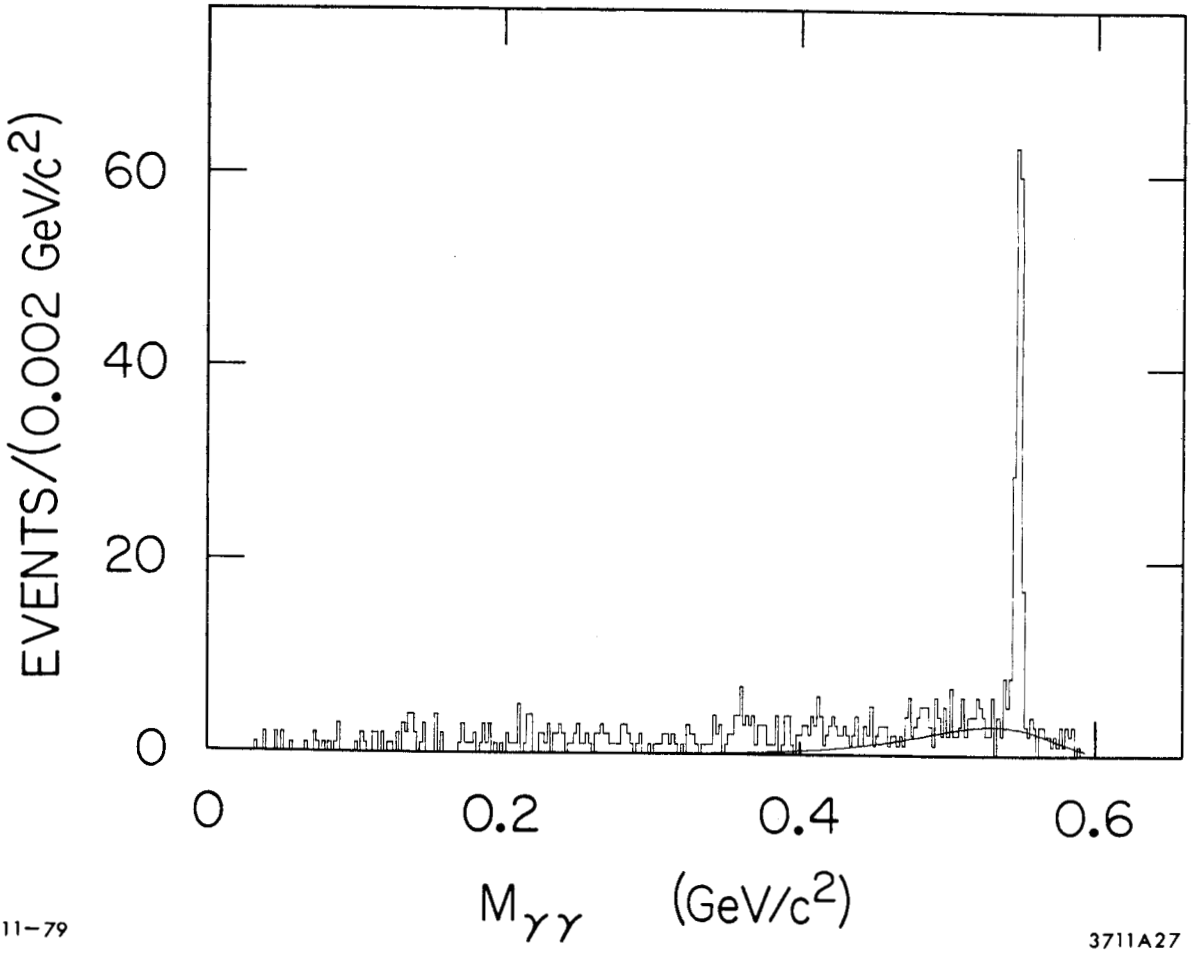

Figure 18: $\gamma\gamma$ mass distribution. The smooth curve shows the expected background from $\psi' \to \pi^0\pi^0\psi$.

5.3 $\psi' \to \gamma\chi$, $\chi \to \gamma\psi$

To see $\psi' \to \gamma\chi$, $\chi \to \gamma\psi$ we remove the $\psi' \to \eta\psi$ events by cutting out events with $0.540 < \gamma\gamma$ mass < 0.556 GeV/c^2. Since each event has two photons, two $\gamma\psi$ masses can be formed. Figure 19 is a scatter plot of the high mass combination versus the low mass combination. The known χ states are expected to appear in the high mass projection. Two peaks are seen, along with their kinematic reflections in the low mass projection. The solid line is a fit to the spectrum using two peaks whose masses and magnitudes are allowed to vary but whose shapes are fixed to the known resolution function. The shape of the background is fixed to that expected from $\pi^0\pi^0\psi$, but its magnitude is allowed to vary (the number of background events found in this way is 9% less than the Monte Carlo prediction). The dashed line in the high mass projection is the background determined in this way. The masses and branching ratios are given in Table 2. Again, the acceptance is determined with the Monte Carlo and the main source of systematic error is the photon detection efficiency. Two errors are given for the masses. The first is the statistical error. The second results from the 0.004 GeV/c^2 uncertainty in the ψ and ψ' masses. The kinematic fit actually determines $A=(M_\chi - M_\psi)/(M_{\psi'} - M_\chi)$. We use 3.09500 and 3.68400 GeV/c^2 for the ψ and ψ' masses. Different values of the ψ and ψ' masses make our χ mass measurements change to keep A constant. The statistical errors dominate other systematic errors.

There is no evidence in Figure 19 for other intermediate states. We are insensitive to the state at 3.60 Gev/c^2 reported by the DESY-Heidel-

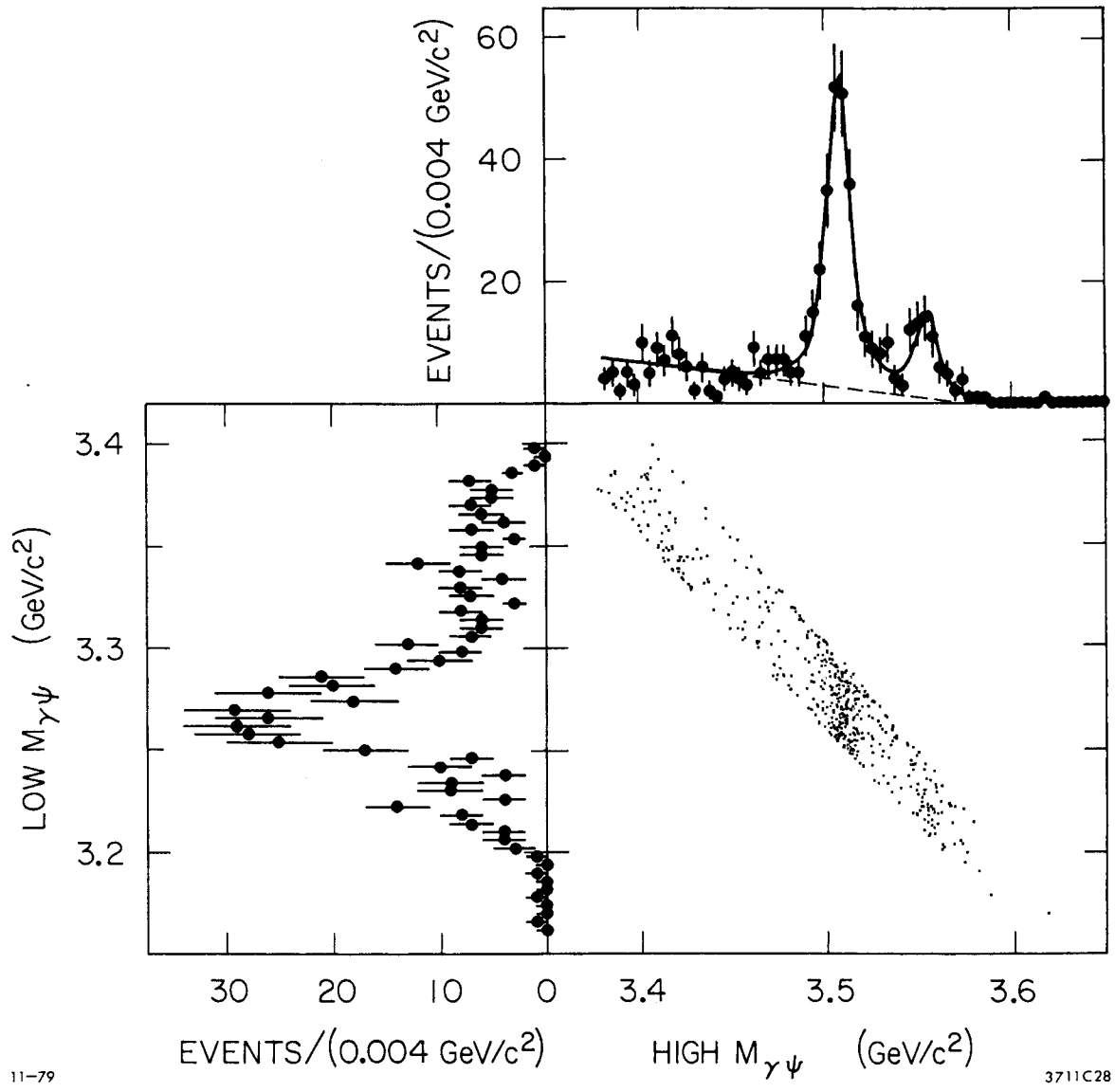

Figure 19: Scatterplot of the higher $\gamma\psi$ mass vs. the lower $\gamma\psi$ mass.

TABLE 2

Branching ratios for the decay $\psi' \to \gamma\chi \to \gamma\gamma\psi$.

The branching ratio for $\chi \to \gamma\psi$ is obtained using previous measurements (7±2)% for the branching ratio $\psi' \to \gamma\chi$.

mass (GeV/c^2)	events	(B.R. $\psi' \to \gamma\chi$)$\cdot$ (B.R. $\chi \to \gamma\psi$) (%)		(B.R. $\chi \to \gamma\psi$) (%)
3.410	<40	<0.56	(90% C.L.)	<8.
3.455	<11	<0.13	(90% C.L.)	
3.5081±0.0006±0.0040	254±31	2.4±0.6		34.±13
3.555±0.001±0.004	69±11	1.1±0.3		16.±6

berg group[20] because our efficiency for a 0.090 GeV photon is very low. Table 2 gives branching ratio limits for states at 3.410 and 3.455 GeV/c^2. The former is well established by its hadronic decay modes and by its presence in the inclusive photon spectrum.

Only one experiment has published a branching ratio for a $\chi(3455)$.[21] Others have had a few candidate events there[22] but have not published branching ratios. In the work of Ref. 21, the $\chi(3455)$ was observed in the decay $\psi' \to \gamma\gamma\psi$ where one of the two photons was observed by its pair conversion while detection of the second photon was not required. There were 4 events in the signal where one background event was expected in

---

[20] W. Bartel et al., Phys. Lett. 79B, 492 (1978).

[21] W. Tanenbaum et al., Phys. Rev. D17, 1731 (1978).

[22] B. H. Wiik and G. Wolf, DESY 78/23, 79 (1978).

the whole scatterplot. The published branching ratio is a factor of 6 higher than our limit. Since the present experiment has higher statistics and a good understanding of the backgrounds, it seems probable that the old signal was an unfortunate statistical fluctuation. Note that in contrast to the other χ states, the $\chi(3455)$ has not been observed in hadron decays or inclusively.

The $\chi(3455)$ had been associated with the expected 2^1S_0 state, the η_c'. With this assignment, measured branching ratios differed from theoretical predictions by an order of magnitude.[23] This new limit means the $\chi(3455)$ is no longer a candidate for the η_c', removing these difficulties.

5.4 $\psi' \to \pi^0 \psi$

The decay $\psi' \to \pi^0 \psi$ violates isospin conservation and hence is expected to have a very small branching ratio. To detect it, one needs good resolution and low background. With the 5-constraint fit, the π^0 mass resolution is ± 0.004 GeV/c^2. Most of the non-eta events in Figure 18 come from $\psi' \to \gamma\chi$, $\chi \to \gamma\psi$ (the $\gamma\gamma$ mass distribution from χ events is roughly proportional to the $\gamma\gamma$ mass). These χ events are removed by cutting out all events with high $\gamma\psi$ mass greater than 3.488 GeV/c^2. The resulting $\gamma\gamma$ mass spectrum is shown in Figure 20a. There is a small peak at the π^0 mass. To reduce the background still further, 4 other cuts are applied. First we require the measured energy of both photons to be

---

[23] Herwig Schopper, DESY 77/79 (1977).

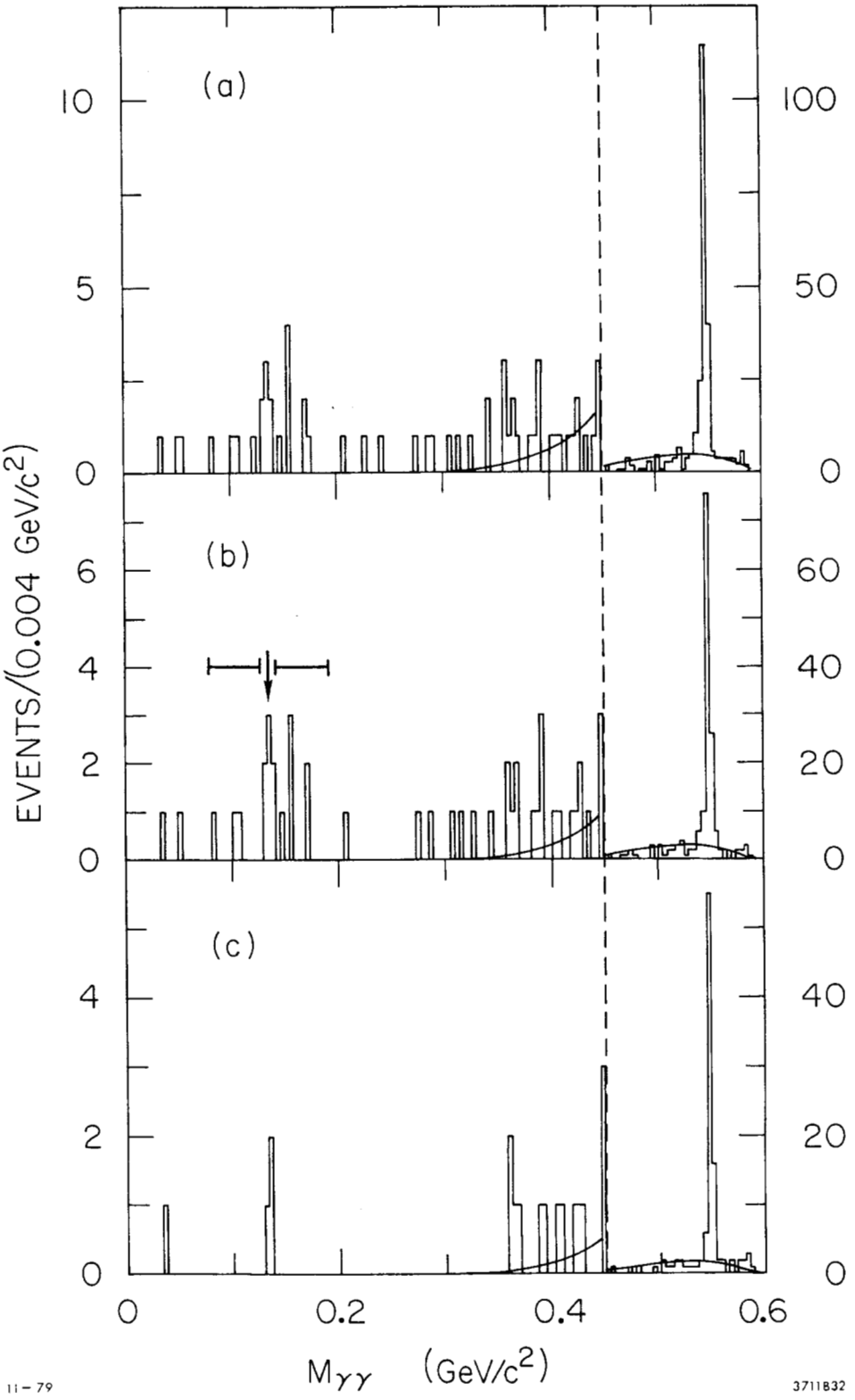

Figure 20: $\gamma\gamma$ mass distribution with χ's removed. The different cuts used for a, b, and c are explained in the text. Note that the η peak is scaled down by a factor of 10. The arrow points to the π^0 mass. The inner tick marks show the signal region. The region between the inner and outer tick marks indicates the region used to estimate the background.

more than 0.14 GeV. This reduces background from false photons while having little effect on the π^0 detection efficiency. This cut was not used before because it would cut out the decay $\psi' \to \gamma\chi(3.550)$ which gives a 0.13 GeV photon. Second, events where the difference in azimuthal angle of the two leptons is greater than 178.5^0 are cut out. This reduces background from $e^+e^- \to e^+e^-$ where the initial or final state electrons radiate a photon. This cut was not used before because in the decay, $\psi' \to \eta\psi$, the ψ is nearly at rest. Therefore the leptons from its decay are nearly back-to-back and often fail this cut. Third, photons which use a strip in the calorimeter that is also used by a charged track are cut out. This is done because the pattern recognition program is more likely to find a false photon when one strip has real pulse-height on it. Fourth, events which have a photon with energy > 0.175 GeV in addition to the 2 photons used in the fit are cut out. This helps reduce background from $\psi' \to \pi^0\pi^0\psi$. The 0.175 GeV requirement helps keep false photons (see Figure 5) from causing real $\psi' \to \gamma\gamma\psi$ events from being lost. The third and fourth cuts were not used before because of the difficulty of estimating the fraction of signal events lost. These cuts introduce systematic errors in the branching ratio measurements. For the case $\psi' \to \pi^0\psi$, the statistical errors are large enough so that this systematic error is not important. Also, we measure the fraction of signal events lost by these cuts by noting their effect on the signal $\psi' \to \eta\psi$.

Figure 20b shows the resulting $\gamma\gamma$ mass spectrum. Taking the ± 6 MeV/c^2 region around the π^0 mass as the signal (the expected resolution is 4 MeV/c^2), and the 48 MeV/c^2 region on each side as background, 7

events are observed where the expected background is 1.1. The probability that this background could fluctuate upwards to 7 events is $1.5 \cdot 10^{-4}$. Further evidence that these 7 events are not background comes from their flat χ^2 probability distribution (Figure 21). A signal should have a flat χ^2 probability distribution while, as shown in the figure, background tends to peak at low probability.

The narrow width of the signal helps exclude the possibility of a missing particle, for example, $\psi' \to \gamma\pi^0\psi$. A Monte Carlo study of this process shows that if a 0.025 GeV/c photon is missing, the peak shifts to 0.140 GeV/c^2 which is inconsistent with the data. A Monte Carlo study of the $\psi' \to \pi^0\pi^0\psi$ background gives no events with mass less than 0.330 GeV/c^2. Hence any missing particle must be a photon or neutrino of less than 0.025 GeV.

In Figure 20b the remaining events at low $\gamma\gamma$ mass come from $\chi(3510)'$s in the non-Gaussian tail of the peak. Removing all events with high $\gamma\psi$ mass > 3.448 GeV/c^2 results in Figure 20c. Three signal events remain with essentially no background.

Attributing the signal to the reaction $\psi' \to \pi^0\psi$, we calculate the branching ratio. There are 5.9±2.6 signal events. The acceptance (including $B(\psi \to \ell^+\ell^-)$) calculated with the Monte Carlo is (0.43±0.09)%. An additional factor of 0.90 coming from cuts 3 and 4 above is obtained from noting the decrease in the η signal caused by these cuts. The resulting branching ratio for $\psi' \to \pi^0\psi$ is (0.15±0.06)%. The ratio $\Gamma(\psi' \to \pi^0\psi)/\Gamma(\psi' \to \eta\psi)$ is 0.06±0.02.

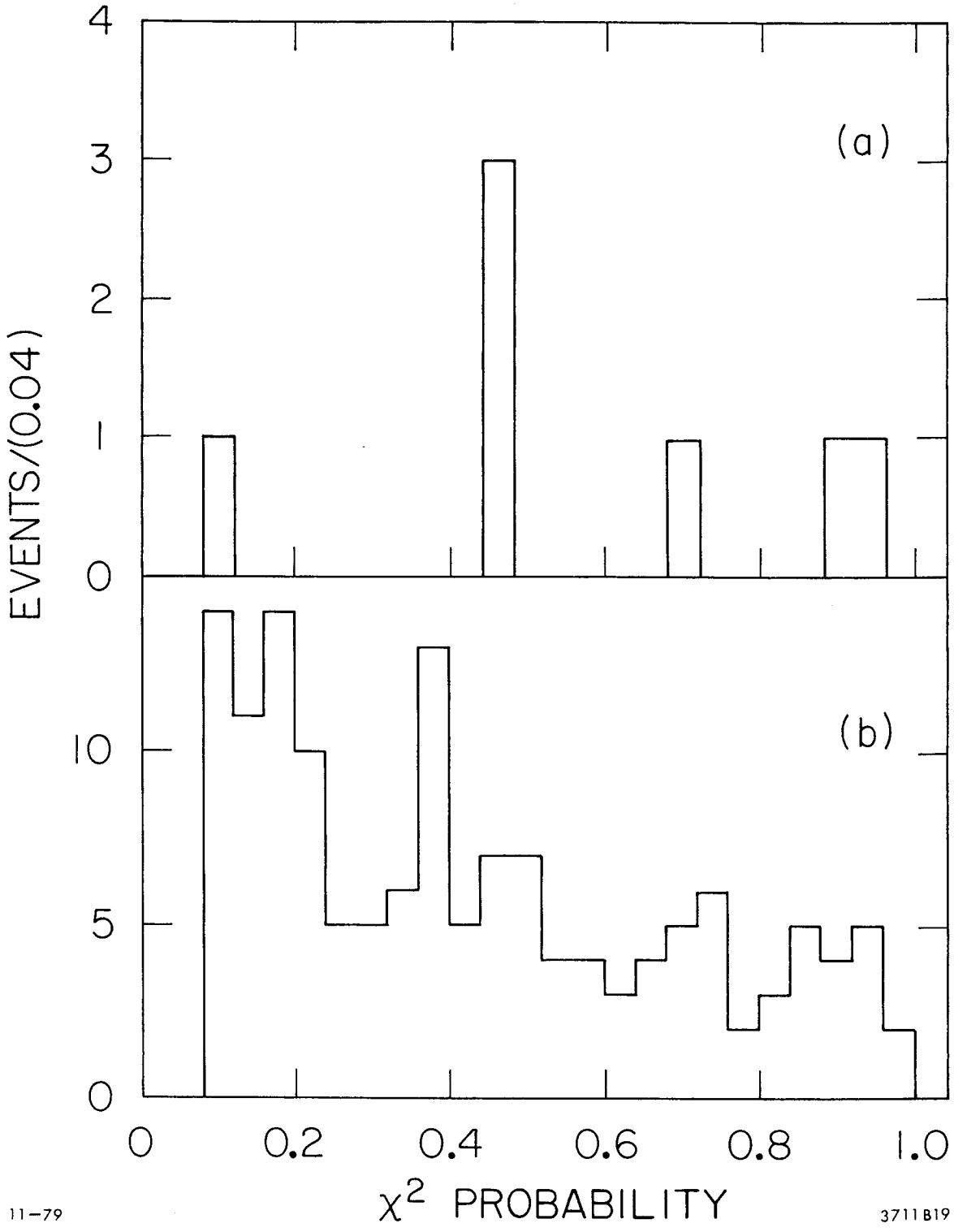

Figure 21: χ^2 probability distribution for $\psi' \to \pi^0 \psi$ events. (b) for events which have no η's or χ's or π^0's.

Another possible source of the signal is the nonresonant decay of the virtual photon directly to $\pi^0\psi$. About 7% of the hadronic events at the ψ' energy come from virtual photon decays. It would have to have a branching ratio of 0.15/0.07=2.1% to cause the signal. Typical branching ratios of e^+e^- to an exclusive final state are small (e.g. $B(e^+e^-\to\rho^+\rho^-) < B(e^+e^-\to 2\pi^+2\pi^-) = 2\%$[24]) and the decay $e^+e^-\to\pi^0\psi$ is Zweig suppressed, which typically suppresses decays by a factor of 1000. So a reasonable estimate for $B(e^+e^-\to\pi^0\psi)$ is less than 0.002%, a factor of 1000 below the observed signal strength.

Several papers have been published predicting the $\psi'\to\pi^0\psi$ branching ratio.[25] The calculation involves mixing of the SU(3) symmetric π^0, η, and η' states to form the physical π^0, η, and η' states. These calculations show that the QED contribution to this mixing is small, making the decay $\psi'\to\pi^0\psi$ a good place to study strong interaction violations of SU(2) (isospin) and SU(3) symmetries. Basically, these violations occur because the masses of the u, d, and s quarks in the strong interaction Hamiltonian are not equal. More recent work[26] where effects of symmetry breaking in the decay amplitude are included in the calculation gives $\Gamma(\psi'\to\pi^0\psi)/\Gamma(\psi'\to\eta\psi) = 0.04\pm0.010$ consistent with this experiment.

---

[24] B. Jean-Marie et al., preprint SLAC-PUB-1711.

[25] G. Segre and J. Weyers, Phys. Lett. 62B, 91 (1976); N. Deshpande and E. Ma, Phys. Lett. 69B, 343 (1977); H. Genz, Nuovo Cim. Lett. 21, 270 (1978); R. Bhandari and L. Wolfenstein, Phys. Rev. D17, 1852 (1978).

[26] P. Langacker, preprint SLAC-PUB-2434.

Chapter VI

HADRONIC χ DECAYS

It is interesting to observe decays of the form $\psi' \to \gamma\chi$, $\chi \to$ hadrons for several reasons. The three established χ states can be observed in this decay, allowing studies of their decay modes and providing information on their quantum numbers. It may also be possible to observe the η_c or η_c' in this way. To enhance this possibility we have attempted to measure all final states for which the Mark II detector has a reasonable acceptance. Information on the quantum numbers of the χ's can be obtained by measuring the angular distribution of the photon and by observing decays which are forbidden for particles with certain quantum numbers.

6.1 EVENT SELECTION

Figure 22 shows a typical completely detected hadronic χ decay. The event selection criteria are similar for all the decay modes, so the general technique will be described without reference to the specific decay modes. There must be the proper number of charged tracks passing within $r<0.06$ m and $|z|<0.15$ m of the origin. Detection of the photon is not required. Events where any of these tracks have $p_t<0.1$ GeV/c or $|\cos\theta|>0.76$ are not used. If there is no good TOF information for a track, it is assumed to be a pion. For tracks with good TOF information π, K or proton hypotheses are tried if the measured flight time is

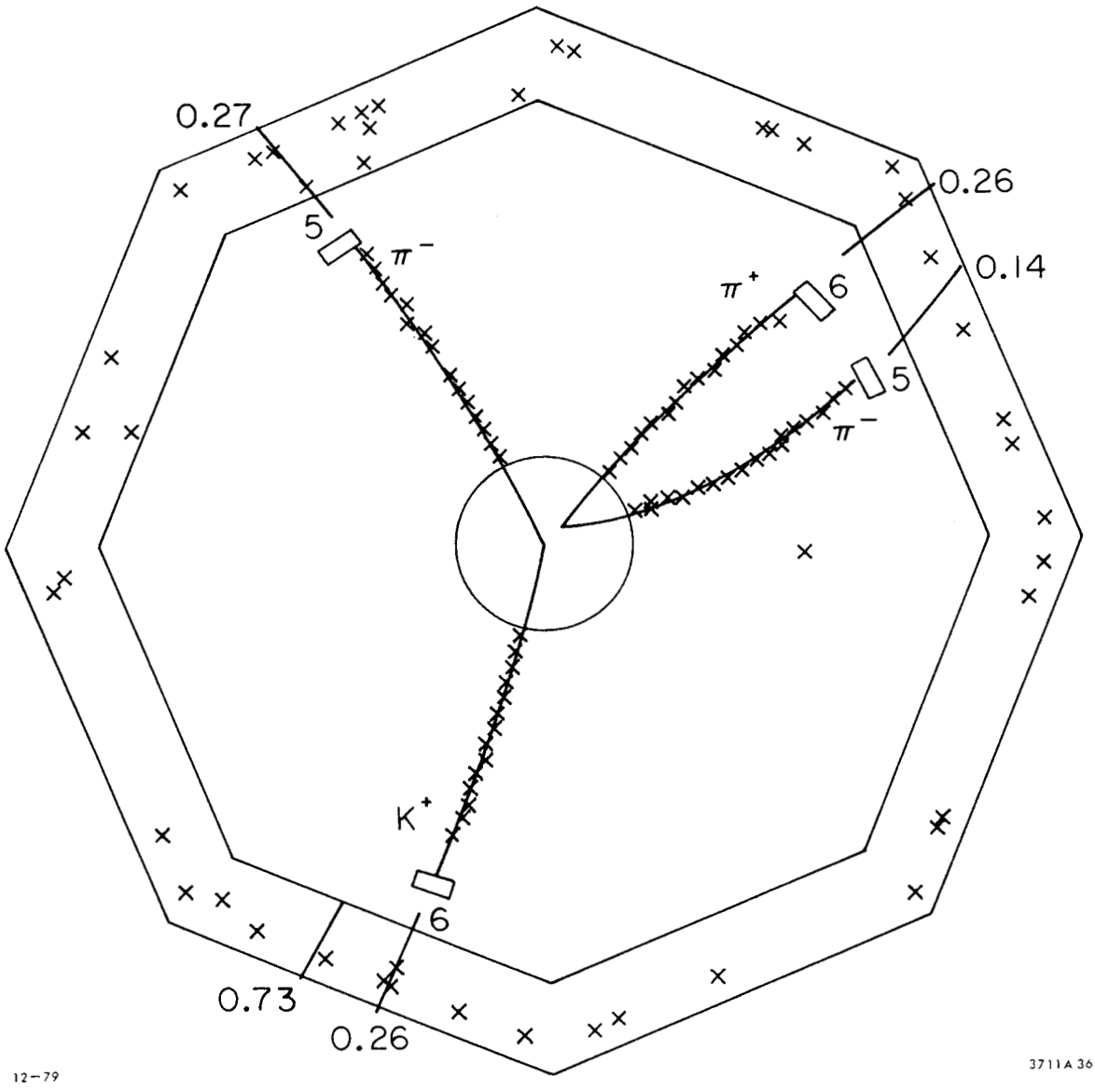

Figure 22: Picture of $\psi' \to \gamma\eta_c(2970)$, $\eta_c \to \pi^- K^+ K_s$. The K_s travels several centimeters before decaying to $\pi^+\pi^-$.

within 0.78 ns of the expected flight time (this is a 2.6σ, 1% confidence level cut). Multiple mass hypotheses are allowed for particles. For each set of particle identities that satisfies conservation of charge, baryon number, and strangeness, a recoil mass squared is calculated. If its magnitude is less than 0.1 $(Gev/c^2)^2$ (a very loose cut) a 1 constraint kinematic (SQUAW) fit is done which constrains the recoil mass to zero (the photon mass). If an event has more than one successful fit, the one with the smallest total χ^2 (sum of SQUAW χ^2 and TOF χ^2) is used. In this way, the particle identification ambiguities are resolved. Events with SQUAW χ^2 probability less than 0.1 are rejected.

The remaining cuts are designed to remove specific backgrounds. The most serious backgrounds for 2 particle decays of the χ's are $e^+e^-\rightarrow e^+e^-$ and $e^+e^-\rightarrow\mu^+\mu^-$. These backgrounds are reduced by requiring both particles to be identified by the muon system as not being muons and by the liquid argon system as not being electrons. Candidates for $\chi\rightarrow\bar{p}p$ are not removed with these cuts if one of the particles is unambiguously labeled as a proton by TOF (TOF > (expected TOF for a kaon)+0.78 ns). A background to $\chi\rightarrow\pi^+\pi^-\pi^+\pi^-$ or $\pi^+\pi^-K^+K^-$ is $\psi'\rightarrow\pi^+\pi^-\psi$ or $\psi'\rightarrow\eta\psi$ where $\psi\rightarrow\ell^+\ell^-$. This background is reduced by removing events with a mass recoiling against any $\pi^+\pi^-$ pair that is greater than 3.07 GeV/c^2. Finally, a background to other hadronic decay modes from $\psi'\rightarrow\pi^+\pi^-\psi$, $\psi\rightarrow$hadrons is reduced by removing events that have a mass recoiling against any $\pi^+\pi^-$ pair between 3.07 and 3.11 GeV/c^2. The unshaded histograms in Figure 23 show the resulting spectra for the decay modes in which signals are observed.

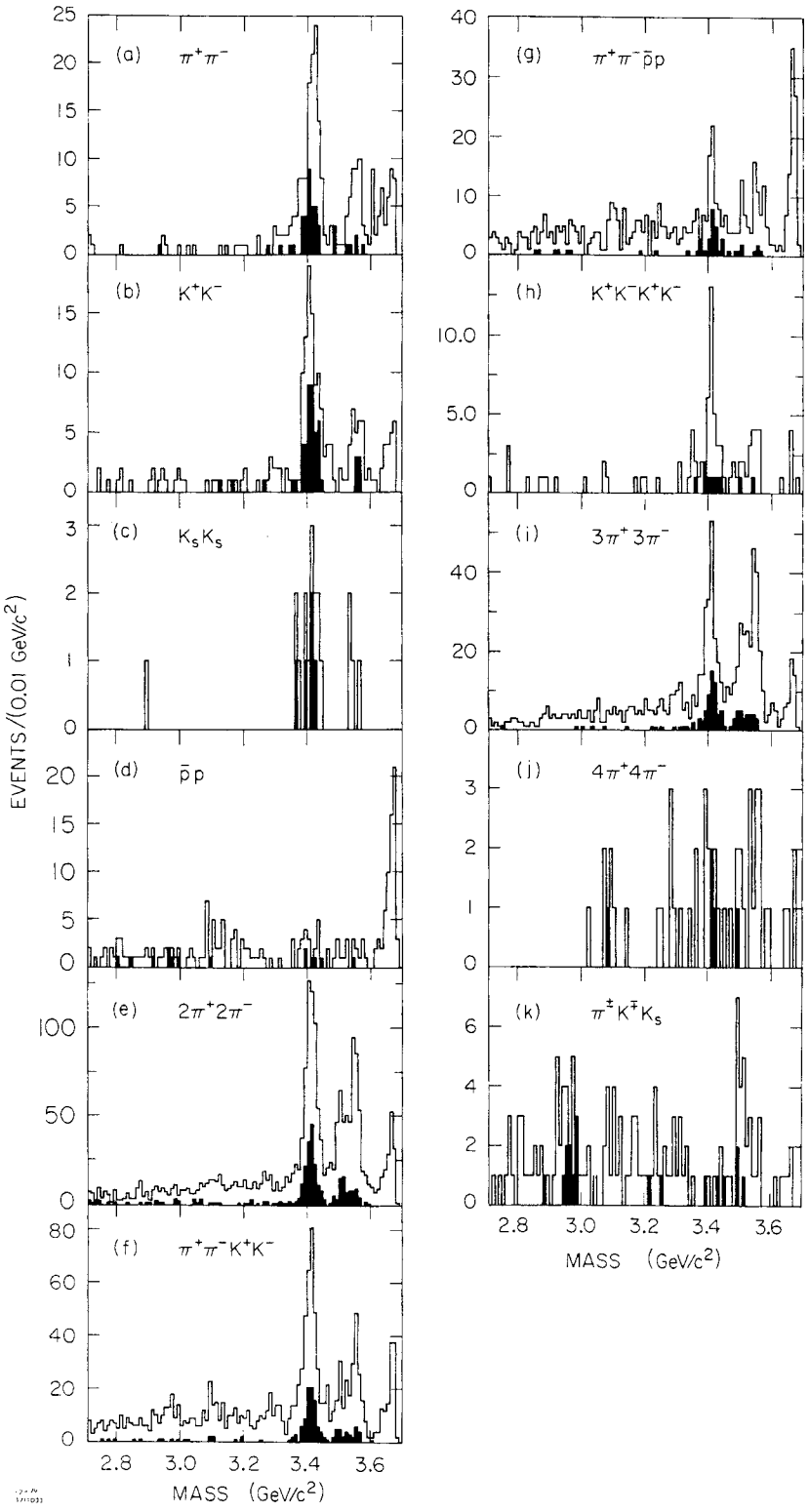

Figure 23: Mass spectra from fits to $\psi' \to \gamma$+hadrons. The unshaded and shaded spectra come from 1-C and 4-C fits, respectively.

The shaded histograms in the figure are the result of an identical analysis where detection of the photon is required and a 4 constraint kinematic fit (conservation of energy and momentum) is done. These 4-C fits have less background and better resolution, but smaller acceptance than the 1-C fits.

6.2 BRANCHING RATIOS

Peaks are observed at 4 masses in the above spectra. The peaks at 3.67 GeV/c^2 come from direct ψ' decays to hadrons. The SQUAW fit shifts the mass down slightly from the ψ' mass of 3.684 GeV/c^2. In most of the spectra there are clear peaks coming from decays of the $\chi(3415)$, $\chi(3510)$, and $\chi(3555)$.

To obtain branching ratios from these spectra, the Monte Carlo is used to determine the acceptance. A phase space distribution is used to model the $\chi(3510)$, $\chi(3555)$, and $\eta_c(2970)$ decays. For the $\chi(3415)$ the photon is produced with a $1+\cos^2\theta$ angular distribution. To check for model dependence, the acceptance for $\chi(3415)\rightarrow\pi^+\pi^-\rho$, $\rho\rightarrow\pi^+\pi^-$ was also calculated. It differs from the acceptance for $\chi(3415)\rightarrow\pi^+\pi^-\pi^+\pi^-$ by a factor of 0.96±0.02. This 4% difference is added in quadrature to the systematic error calculated from section 4.2.0 to obtain the total systematic error of the acceptance calculation. This total systematic error is always less than 0.7 of the statistical error. The Monte Carlo is also used to determine the probability that events are misclassified (e.g. a $\chi\rightarrow4\pi$ event is put into the $\chi\rightarrow2\pi2k$ histogram). The decays $\chi\rightarrow\pi^+\pi^-$ and $\chi\rightarrow K^+K^-$ are confused 10% of the time. Misidentification probabili-

ties are negligible for all other decay modes. The branching ratios are corrected for this misidentification.

The number of detected events is determined by fitting the spectra between 3.2 and 3.62 GeV/c^2 to a linear background plus three peaks. The masses of the $\chi(3510)$ and $\chi(3555)$ are fixed to 3 and 5 MeV/c^2 below those determined from the decay $\psi' \to \gamma\gamma\psi$ (Table 2). They are fixed lower than the actual masses because the 1-C SQUAW fits shift the peaks downwards. The mass of the $\chi(3415)$ is allowed to vary in each fit. The shapes of the peaks are fixed to the known resolution function and the x-intercept of the linear background is fixed to that determined by a Monte Carlo of the principle background: $\psi' \to \pi^0$+charged hadrons. The resulting fits for two of the decay modes are shown in Figure 24. The fitted masses for the $\chi(3415)$ are shown in Table 3. The errors on the separate mass measurements are statistical. The first error on the average mass is statistical and the second error results from the 4 MeV/c^2 uncertainty in the ψ' mass. Our $\chi(3415)$ mass measurement is directly proportional to the ψ' mass we use (3.68400 GeV/c^2).

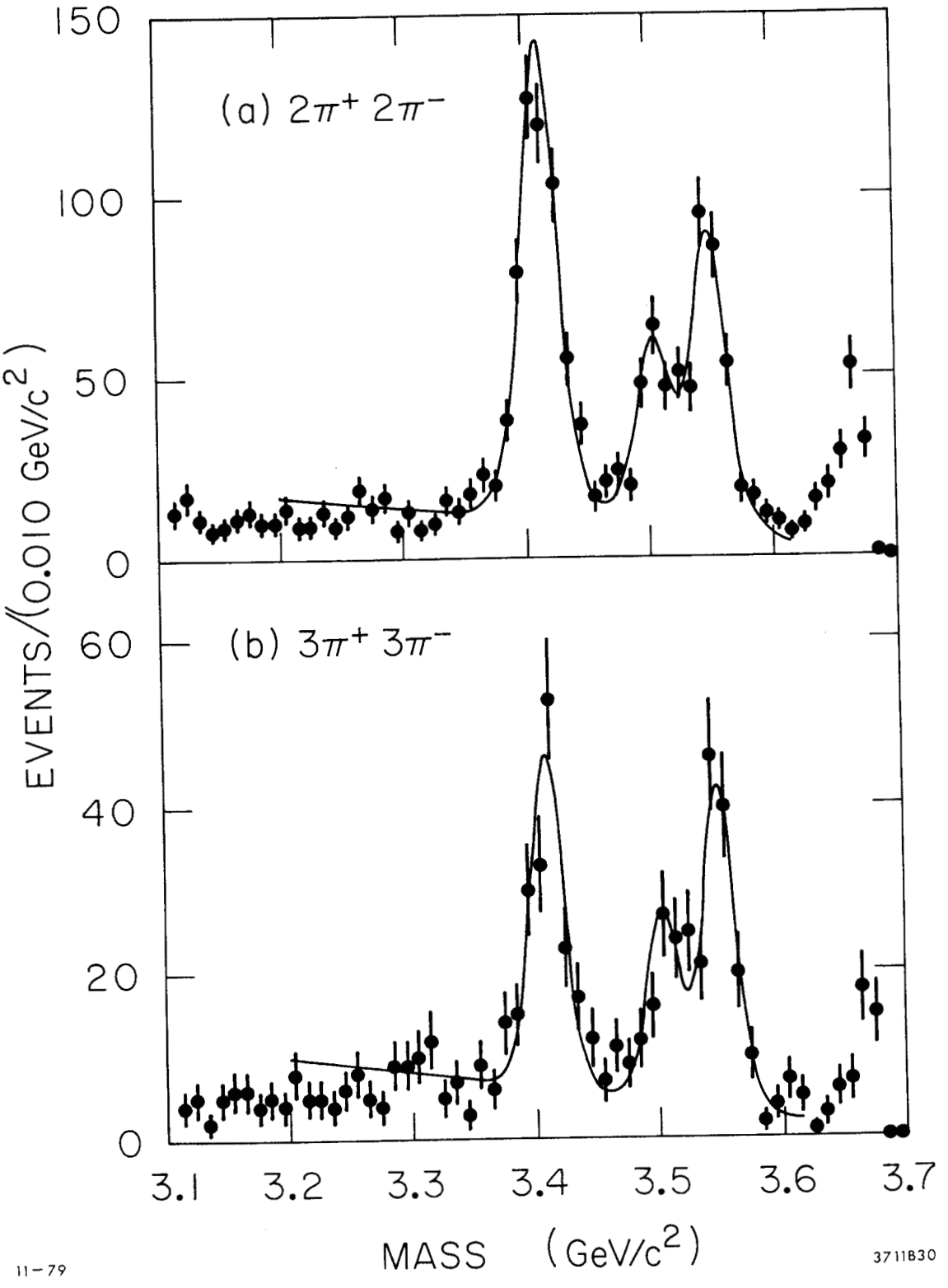

Figure 24: Fits of the 1-C χ mass spectra

TABLE 3

Mass of the $\chi(3415)$

mode	mass (MeV/c^2)
$\pi^+\pi^-$	3415±2
K^+K^-	3414±2
$2\pi^+2\pi^-$	3413±1
$\pi^+\pi^-K^+K^-$	3412±1
$\pi^+\pi^-pp$	3414±2
$2K^+2K^-$	3416±3
$3\pi^+3\pi^-$	3411±2
average	3412.9±0.6±4.0

Since the spectra from the 1-C fits have higher statistics and smaller systematic errors than the 4-C spectra, they are used to determine all the χ branching ratios except $\chi\to\bar{p}p$ (where the 1-C fit shows no significant signal above the background). The η_c branching ratios and limits are obtained from the 4-C spectra since they have a smaller background and the efficiency for a 0.7 GeV photon is near 1. The η_c limits are calculated at a mass of 2.970 GeV/c^2, the value recently measured by the Crystal Ball experiment.[27] The limits are similar for all masses within 0.2 GeV/c^2 of this mass. The resulting branching ratios and limits are shown in Table 4. We have looked for many other decay modes,

---

[27] E. Bloom, to be published in the proceedings of the Photon-Lepton Symposium at Fermilab (1979).

including decays with a π^0 or an η, but the branching ratio limits are too high to be of use.

Also shown in the table are the results of a calculation using the statistical model.[28] This model assumes all available isospin states are populated with their statistical weights to relate the rates for decays to different charge states of a general decay mode. For example it relates $B(\chi\to\pi^0\pi^0)$ to $B(\chi\to\pi^+\pi^-)$ but does not relate these to $B(\chi\to K^+K^-)$. The last column in the table gives the ratio of the rate for the observed decay mode to the rate for the general decay mode. It also gives the branching ratios for the general decay mode. The bottom lines of the table give the sums of the branching ratios to the observed general decay modes. Only 1/2 of the χ decays have been observed. The reliability of this estimate is not very good since the statistical model is very simple and is certainly not completely correct.

Some of the above χ hadronic decays have been previously observed.[29] This is the first report of decays to K_sK_s, $\bar{p}p$, $2K^+2K^-$, $4\pi^+4\pi^-$, and $\pi^\pm K^\mp K_s$. This last decay is important because a particle with $J=0^+$ is not allowed to decay to $\pi^\pm K^\mp K_s$. The absence of a peak for the $\chi(3415)$ is further support for its quantum number assignment of 0^+, while the observation of the $\chi(3510)$ decaying in this way shows that it is not 0^+. This last fact was already known from observations of the angular dis-

---

[28] A. Pais, Ann. Phys. 9, 548 (1960).

[29] W. Tanenbaum et al., Phys. Rev. D17, 1731 (1978).

[30] ibid.

$K^+\bar{p}\Lambda + K^-p\bar{\Lambda}$					
2970	<2.3	$<6.2\cdot10^{-4}$		$<1.7\cdot10^{-1}$	
3415	$<9.$	$<1.2\cdot10^{-3}$		$<1.7\cdot10^{-2}$	
3510	<3.9	$<5.3\cdot10^{-4}$		$<7.6\cdot10^{-3}$	
3555	<6.5	$<8.9\cdot10^{-4}$		$<1.3\cdot10^{-2}$	
$2\pi^+2\pi^-$					2/5
2970	$<5.$	$<4.8\cdot10^{-5}$		$<1.4\cdot10^{-2}$	
3415	504±44	$(2.1\pm0.2)\cdot10^{-3}$	10^{-346}	$(3.0\pm0.3)\cdot10^{-2}$	$(7.5\pm0.8)\cdot10^{-2}$
3510	193±22	$(8.2\pm1.0)\cdot10^{-4}$	10^{-103}	$(1.2\pm0.1)\cdot10^{-2}$	$(3.0\pm0.4)\cdot10^{-2}$
3555	313±29	$(1.3\pm0.1)\cdot10^{-3}$	10^{-240}	$(1.9\pm0.2)\cdot10^{-2}$	$(4.8\pm0.5)\cdot10^{-2}$
$\pi^+\pi^-K^+K^-$					1/4
2970	<3.3	$<5.4\cdot10^{-5}$		$<1.5\cdot10^{-2}$	
3415	262±28	$(1.9\pm0.2)\cdot10^{-3}$	10^{-144}	$(2.7\pm0.3)\cdot10^{-2}$	$(6.8\pm0.8)\cdot10^{-2}$
3510	60±12	$(4.0\pm0.8)\cdot10^{-4}$	10^{-18}	$(5.7\pm1.1)\cdot10^{-3}$	$(1.4\pm0.3)\cdot10^{-2}$
3555	126±16	$(8.2\pm1.1)\cdot10^{-4}$	10^{-65}	$(1.2\pm0.2)\cdot10^{-2}$	$(3.0\pm0.4)\cdot10^{-2}$
$\pi^+\pi^-\bar{p}p$					1/4
2970	<4.3	$<5.2\cdot10^{-5}$		$<1.5\cdot10^{-2}$	
3415	46±10	$(2.6\pm0.6)\cdot10^{-4}$	10^{-16}	$(3.7\pm0.8)\cdot10^{-3}$	$(1.5\pm0.3)\cdot10^{-2}$
3510	19±6	$(1.1\pm0.3)\cdot10^{-4}$	$3\cdot10^{-6}$	$(1.6\pm0.4)\cdot10^{-3}$	$(6.4\pm0.2)\cdot10^{-3}$
3555	36±8	$(2.3\pm0.5)\cdot10^{-4}$	10^{-17}	$(3.3\pm0.7)\cdot10^{-3}$	$(1.3\pm0.3)\cdot10^{-2}$
$2K^+2K^-$					1/6
2970	<2.3	$<8.7\cdot10^{-5}$		$<2.5\cdot10^{-2}$	
3415	28±10	$(4.4\pm1.6)\cdot10^{-4}$	10^{-22}	$(6.\ \pm2.\ )\cdot10^{-3}$	$(3.8\pm1.4)\cdot10^{-2}$
3510	6±4	$(8.5\pm5.7)\cdot10^{-5}$	$1\cdot10^{-3}$	$(1.2\pm0.8)\cdot10^{-3}$	$(7.\ \pm5.\ )\cdot10^{-3}$
3555	14±6	$(2.0\pm0.9)\cdot10^{-4}$	$1\cdot10^{-10}$	$(2.9\pm1.2)\cdot10^{-3}$	$(1.7\pm0.7)\cdot10^{-2}$
$3\pi^+3\pi^-$					4/21
2970	<2.9	$<8.7\cdot10^{-5}$		$<2.5\cdot10^{-2}$	
3415	136±19	$(1.8\pm0.3)\cdot10^{-3}$	10^{-66}	$(2.5\pm0.4)\cdot10^{-2}$	$(1.3\pm0.1)\cdot10^{-1}$
3510	78±13	$(9.0\pm1.5)\cdot10^{-4}$	10^{-31}	$(1.3\pm0.2)\cdot10^{-2}$	$(6.8\pm1.1)\cdot10^{-2}$
3555	132±17	$(1.7\pm0.3)\cdot10^{-3}$	10^{-81}	$(2.4\pm0.4)\cdot10^{-2}$	$(1.3\pm0.2)\cdot10^{-1}$
$2\pi^+2\pi^-K^+K^-$					1/9
2970	<2.3	$<2.2\cdot10^{-4}$		$<6.3\cdot10^{-2}$	
3415	$<45.$	$<2.0\cdot10^{-3}$		$<2.9\cdot10^{-2}$	
3510	$<9.$	$<4.1\cdot10^{-4}$		$<5.9\cdot10^{-3}$	
3555	$<10.$	$<4.5\cdot10^{-4}$		$<6.4\cdot10^{-3}$	
$\pi^+\pi^-2K^+2K^-$					
2970	<2.3	$<2.5\cdot10^{-3}$		$<7.0\cdot10^{-1}$	
3415	<5.5	$<3.1\cdot10^{-3}$		$<4.4\cdot10^{-2}$	
3510	<2.9	$<1.6\cdot10^{-3}$		$<2.3\cdot10^{-2}$	
3555	<3.3	$<1.8\cdot10^{-3}$		$<2.6\cdot10^{-2}$	
$4\pi^+4\pi^-$					10/117
2970	<2.3	$<4.0\cdot10^{-4}$		$<1.1\cdot10^{-1}$	
3415	7±4	$(5.\ \pm3.\ )\cdot10^{-4}$	$3\cdot10^{-4}$	$(8.\ \pm4.\ )\cdot10^{-3}$	$(9.\ \pm5.\ )\cdot10^{-2}$
3510	4±3	$(3.\ \pm2.\ )\cdot10^{-4}$	$2\cdot10^{-2}$	$(4.\ \pm3.\ )\cdot10^{-3}$	$(5.\ \pm4.\ )\cdot10^{-2}$
3555	9±5	$(7.\ \pm4.\ )\cdot10^{-4}$	$1\cdot10^{-6}$	$(1.0\pm0.6)\cdot10^{-2}$	$(12.\pm7.\ )\cdot10^{-2}$

Sum of Hadronic Branching Ratios (Statistical Model)	
2970	$(2.8\pm1.0)\cdot10^{-1}$
3415	$(4.4\pm0.6)\cdot10^{-1}$
3510	$(1.9\pm0.4)\cdot10^{-1}$
3555	$(3.6\pm0.7)\cdot10^{-1}$
Sum of Hadronic and $\chi\to\gamma\psi$ branching ratios	
2970	$(2.8\pm1.0)\cdot10^{-1}$
3415	$(4.7\pm0.6)\cdot10^{-1}$
3510	$(4.2\pm0.9)\cdot10^{-1}$
3555	$(4.3\pm0.8)\cdot10^{-1}$

tributions in $\psi'\to\gamma\psi$, $\chi\to\gamma\psi$.[30] While the decays $\chi\to\pi^+\pi^-$ and $\chi\to K^+K^-$ have been previously observed, the present statistics are much better and conclusively show that the $\chi(3415)$ and $\chi(3555)$ decay in this way while there is no evidence for decays of the $\chi(3510)$ to these final states. Since the possible J^{PC} states for two pseudoscalars are 0^{++}, 1^{--}, 2^{++} etc., the $\chi(3415)$ and $\chi(3555)$ must have these quantum numbers. Of course, all the χ's must have positive charge conjugation since they are reached by radiative transitions from the ψ' which is 1^{--}. So this leaves only 0^{++}, 2^{++}, 4^{++} etc. as possible quantum numbers for the $\chi(3415)$ and $\chi(3555)$. Note that the χ's quantum numbers prohibit their decay to $K_L K_S$, so the K^0K^0 branching ratio is twice the K_SK_S branching ratio given in the table.

Only the $\chi(3415)$ and $\chi(3555)$ have clear decays to $2K^+2K^-$. Figure 25 shows the distribution of the lowest K^+K^- mass in these events. The smooth curves show the phase space distribution. There are clear peaks at the $\Phi(1020)$ mass. For the $\chi(3415)$ 13 of 28 events are in the Φ peak while for the $\chi(3555)$ 10 of 15 events are in the Φ peak. Of the 13 and 10 events with Φ's, in 4 and 2 of the events the other K^+K^- pair also have a Φ mass.

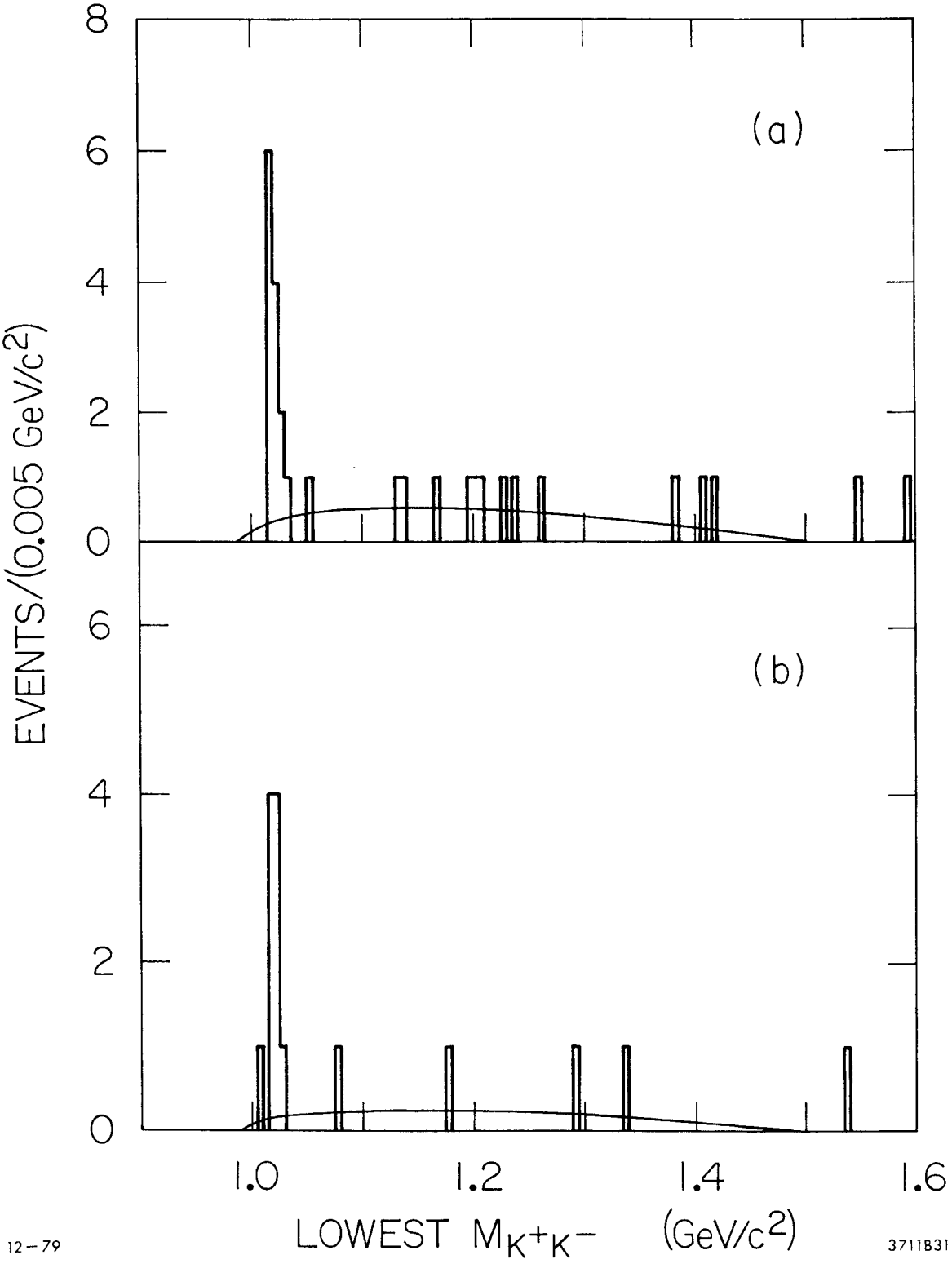

Figure 25: Distribution of lowest K^+K^- mass in χ decays to $2K^+2K^-$: (a) $\chi(3415)$, (b) $\chi(3555)$.

Saving the most interesting result for last, the peak in the 4-C spectrum for $\psi' \to \gamma\chi$, $\chi \to \pi^{\pm}K^{\mp}K_s$ will now be discussed. There are 9 events centered at a mass of 2.97 ± 0.01 GeV/c^2. The width is consistent with the expected resolution of $\sigma = 0.013$ GeV/c^2. There is very little background in the plot. This peak provides strong confirmation for the state observed at 2.98 ± 0.02 GeV/c^2 by the Crystal Ball group.[31] Even though very few of its properties have been measured, we'll refer to this state as the η_c because it is near the mass expected for the η_c. Since $\psi' \to \gamma\eta_c$ the η_c has positive charge conjugation and since $\eta_c \to \pi^{\pm}K^{\mp}K_s$ it cannot be $J^{PC} = 0^+$. Using the Crystal Ball group's measurement of $B(\psi' \to \gamma\eta_c) = (0.35 \pm 0.15)\%$ we obtain $B(\eta_c \to \pi^+K^-K_s) + B(\eta_c \to \pi^-K^+K_s) \approx 9.1\%$. Assuming it decays to K_L's as often as K_s's and using isospin (assuming the η_c has isospin=0) to get $B(\eta_c \to \pi^+K^-K^0) = 2 \cdot B(\eta_c \to \pi^0K^+K^-) = 2 \cdot B(\eta_c \to \pi^0K^0K^0)$ one obtains $B(\eta_c \to \pi KK) = 27\%$. This is a very large branching ratio. None of the other decay modes we investigated show much evidence for the η_c. The second largest signal is in the 4-C $\bar{p}p$ spectrum where there are 3 events near 2.97 GeV/c^2.

---

[31] E. Bloom, to be published in the proceedings of the Photon-Lepton Symposium at Fermilab (1979).

Chapter VII

SUMMARY

The experimental status of the charmonium system has advanced considerably in the last 2 years. It's current status is summarized in Figure 26. Our mass and branching ratio measurements are summarized in tables 5 and 6. The ^3P states: $\chi(3415)$, $\chi(3510)$, and $\chi(3555)$ remain firmly established. The $\chi(3455)$ is effectively dead. Two experiments[32] in addition to our own have set limits on its production in the decay $\psi' \to \gamma\chi$, $\chi \to \gamma\psi$ which is the way it was originally observed. For a short period of time there was a new candidate for the η_c' at a mass of 3.591 GeV/c^2.[33] It was also observed in $\psi' \to \gamma\gamma\psi$. The Crystal Ball experiment[34] has set a limit well below the original measured branching ratio, effectively killing this state. The X(2830) which was observed in the decay $\psi \to 3\gamma$ has also been eliminated by the Crystal Ball experiment. In its place as a candidate for the η_c there is a state at 2.970±0.01 GeV/c^2 observed in the inclusive photon spectrum by the Crystal Ball group and exclusively in its decay to $\pi^{\pm}K^{\mp}K_s$ by this experiment.

---

[32] W. Bartel et al., Phys. Lett. 79B, 492 (1978); E. Bloom, to be published in the proceedings of the Photon-Lepton Symposium, Fermilab (1979).

[33] W. Bartel et al., Phys. Lett. 79B, 492 (1978).

[34] E. Bloom, to be published in the proceedings of the Photon-Lepton Symposium, Fermilab (1979).

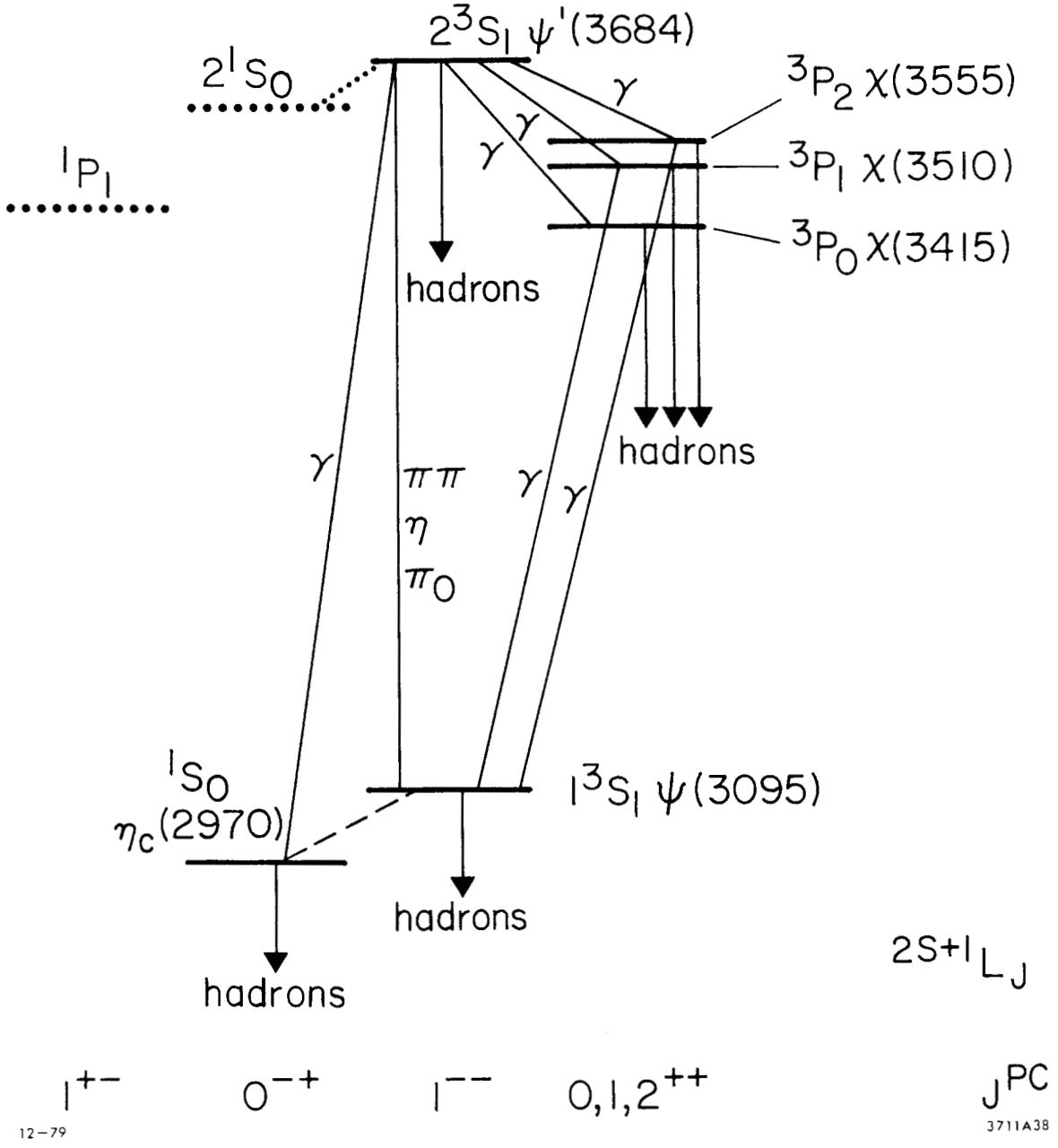

Figure 26: Charmonium level diagram: after. Solid lines indicate things confirmed by experiment. Dashed lines indicate things with a small amount of experimental evidence. Dotted lines indicate things predicted by the Charmonium model for which there is no experimental evidence.

TABLE 5

Masses of the known charmonium states.

The ψ and ψ' masses are not measurements from this experiment; they are the values used in the kinematic fits to obtain the other masses. The errors do not include an overall mass-scale uncertainty of ±4 MeV/c^2.

State	mass (Mev/c^2)
$\eta_c(2970)$	2970. ±10
$\psi(3095)$	3095.00
$\chi(3415)$	3412.9±0.6
$\chi(3510)$	3508.1±0.6
$\chi(3555)$	3555.3±1.1
$\psi'(3684)$	3684.00

TABLE 6

Branching ratios for $\psi'\rightarrow\chi\psi$.

The $\pi\pi\psi$ branching ratios are taken from the Particle Data Group's Review of Particle Properties (1978). Since the number of detected $\pi^+\pi^-\psi$ events was used for normalization, all other branching ratios in this table are proportional to $B(\psi'\rightarrow\pi^+\pi^-\psi)$. The errors given include this uncertainty.

Decay mode	Total branching ratio (%)	from section
$\pi^+\pi^-\psi$	33. ±3.	
$\pi^0\pi^0\psi$	17. ±2.	
$\eta\psi$	2.8 ±0.4	4.3, 5.2
$\gamma\chi(3415)$, $\chi(3415)\rightarrow\gamma\psi$	<0.56	5.3
$\gamma\chi(3510)$, $\chi(3510)\rightarrow\gamma\psi$	2.4 ±0.6	5.3
$\gamma\chi(3555)$, $\chi(3555)\rightarrow\gamma\psi$	1.1 ±0.3	5.3
$\pi^0\psi$	0.15±0.06	5.4

At this time there is no candidate state for the η_c'. We have no evidence for it, but it could easily hide under the peak from direct ψ'

decays or under the $\chi(3555)$ peak. Theorists can easily adjust the parameters of the charmonium potential to make the η_c' very difficult to observe. The $^1P_1$ state is also unobserved. This is not surprising because it cannot be produced directly in e^+e^- annihilation or in radiative ψ' decays.

With the deaths of the X(2830) and $\chi(3455)$ states, the charmonium model now agrees fairly well with the experimental data. Work is now in progress to extend the model to the upsilon system.

Studies of ψ' decays are interesting not only to gain information about the charmonium system, but also as a clean laboratory to study other decays. Particular examples of this are the study of the $\pi^+\pi^-$ dynamics in the decay $\psi'\to\pi^+\pi^-\psi$ and the observation of the decay $\psi'\to\pi^0\psi$ which violates isospin conservation.